



# LUND UNIVERSITY

## Aluminum droplet combustion studies using spatiotemporal diagnostics

Wu, Zhiyong

2025

*Document Version:*

Publisher's PDF, also known as Version of record

[Link to publication](#)

*Citation for published version (APA):*

Wu, Z. (2025). *Aluminum droplet combustion studies using spatiotemporal diagnostics*. [Doctoral Thesis (compilation), Combustion Physics]. Division of Combustion Physics, Department of Physics, Lund University.

*Total number of authors:*

1

*Creative Commons License:*

CC BY-NC

### General rights

Unless other specific re-use rights are stated the following general rights apply:

Copyright and moral rights for the publications made accessible in the public portal are retained by the authors and/or other copyright owners and it is a condition of accessing publications that users recognise and abide by the legal requirements associated with these rights.

- Users may download and print one copy of any publication from the public portal for the purpose of private study or research.
- You may not further distribute the material or use it for any profit-making activity or commercial gain
- You may freely distribute the URL identifying the publication in the public portal

Read more about Creative commons licenses: <https://creativecommons.org/licenses/>

### Take down policy

If you believe that this document breaches copyright please contact us providing details, and we will remove access to the work immediately and investigate your claim.

LUND UNIVERSITY

PO Box 117  
221 00 Lund  
+46 46-222 00 00



# Aluminum Droplet Combustion Studies Using Spatiotemporal Diagnostics

ZHIYONG WU

DEPARTMENT OF PHYSICS | FACULTY OF ENGINEERING | LUND UNIVERSITY



## Aluminum Droplet Combustion Studies Using Spatiotemporal Diagnostics

# Aluminum Droplet Combustion Studies Using Spatiotemporal Diagnostics

Zhiyong Wu



**LUND**  
UNIVERSITY

DOCTORAL DISSERTATION

Doctoral dissertation for the degree of Doctor of Philosophy (PhD) at the Faculty of Engineering at Lund University to be publicly defended on 28<sup>th</sup> of March at 09.15 in the Rydberg Hall, Department of Physics, Professorsgatan 1, Lund

*Faculty opponent*

Prof. Fabien Halter, University of Orléans

**Organization:** LUND UNIVERSITY

**Document name:** Doctoral dissertation

**Date of issue:** 2025-03-28

**Author(s):** Zhiyong Wu

**Sponsoring organization:**

**Title and subtitle:** Aluminum droplet combustion studies using spatiotemporal diagnostics

**Abstract:**

Aluminum is a promising carbon-free energy carrier. The combustion of aluminum in steam offers a novel method for the simultaneous production of hydrogen and heat through the reaction:  $2\text{Al} + 3\text{H}_2\text{O} = \text{Al}_2\text{O}_3 + 3\text{H}_2 + \text{heat}$ . A comprehensive understanding of the combustion mechanism is crucial for predicting and optimizing the performance of aluminum-fueled devices.

This thesis develops different lab-scale aluminum combustion devices and multiple optical diagnostic techniques for flame characterization. Aluminum combustion setups, ranging from single droplets to collective dust flames, are established to provide stable and controllable research targets. The combustion phenomena are inherently complex due to factors such as spatial scales ranging from nanometers to micrometers, transient processes occurring on millisecond timescales, multi-phase dynamics, and extremely high temperatures. To address these challenges, various spatiotemporal diagnostic methods are employed to study key combustion parameters.

A specially designed platform produces single burning aluminum droplets of initial sizes from around  $100\text{ }\mu\text{m}$  to  $500\text{ }\mu\text{m}$ . The droplets are burning in an adjustable oxidizing environment ranging from an  $\text{H}_2\text{O}/\text{N}_2$  mixture to an  $\text{H}_2\text{O}/\text{N}_2/\text{O}_2$  mixture. The single droplets burning in distinct stages offer unique opportunities for fundamental characterization. Furthermore, a lifted aluminum dust flame is established using aluminum fine powders. This dust flame provides a good target to study flame stabilization, particle-particle interactions, and nano-oxide formation.

Spatiotemporal diagnostic techniques are developed to characterize aluminum flames from different perspectives. First, high-speed incandescence-shadowgraph imaging captures the flame morphology evolution and oxide smoke distribution, simultaneously. The technique determines key parameters, including the flame standoff distance, flame sheet thickness, evaporation rates, and Stefan flow velocity. Second, high-speed RGB pyrometry imaging spatially resolves the surface temperatures of different parts over a burning aluminum droplet and measures the temperature evolution along the wire ignition process and the droplet development process. Then, spatially resolved laser absorption spectroscopy is established to quantify the aluminum atom profile around a burning aluminum droplet. Finally, darkfield and brightfield microscopy quantifies the size and volume of nano-oxide particles in the condensation trail of a jetting aluminum droplet within a dust flame.

With that, the thesis herein contributes key datasets and delivers new knowledge to advance the understanding of aluminum combustion.

**Key words:** Aluminum-steam combustion; Single droplet; Aluminum dust flame; Optical diagnostics; Spatiotemporal characterization;

Classification system and/or index terms (if any)

Supplementary bibliographical information

**Language:** English

**Number of pages:** 194

**ISSN and key title:** 1102-8718

**ISBN:** 978-91-8104-402-7 (print)

**ISBN:** 978-91-8104-403-4 (electronic)

Recipient's notes

Price

Security classification

I, the undersigned, being the copyright owner of the abstract of the above-mentioned dissertation, hereby grant to all reference sources permission to publish and disseminate the abstract of the above-mentioned dissertation.

Signature

Date 2025-02-12

# Aluminum Droplet Combustion Studies Using Spatiotemporal Diagnostics

Zhiyong Wu



**LUND**  
UNIVERSITY

**Thesis main advisor**

Prof. Zhongshan Li

**Thesis co-advisors**

Prof. Marcus Aldén

Dr. Christian Brackmann

Dr. Arman Ahamed Subash

**Cover, front:** A photo of the trajectory of a burning aluminum droplet in a hot steam flow, together with several magnified images of isolated burning aluminum droplets.

**Cover, back:** Photos of aluminum dust flames. Left: pure aluminum powders. Right: aluminum alloy (S260) powders.

**Funding information:** this thesis is financially supported by the Knut and Alice Wallenberg Foundation through COCALD project.

Copyright pp. i-xii and 1-64 © Zhiyong Wu

Paper 1 © the authors. Published by Elsevier Ltd

Paper 2 © the authors. Published by Elsevier Ltd

Paper 3 © the authors (Manuscript unpublished)

Paper 4 © the authors (Manuscript unpublished)

Paper 5 © the authors. Published by Elsevier Ltd

Paper 6 © the authors. Published by Elsevier Ltd

Paper 7 © the authors. Published by Elsevier Ltd

Lund University

Faculty of Engineering

Department of Physics

Lund Reports on Combustion Physics, LRCP-264

ISBN 978-91-8104-402-7 (print)

ISBN 978-91-8104-403-4 (electronic)

ISSN 1102-8718


ISRN LUTFD2/TFCP-264-SE

Printed in Sweden by Media-Tryck, Lund University

Lund 2025



Media-Tryck is a Nordic Swan Ecolabel certified provider of printed material. Read more about our environmental work at [www.mediatryck.lu.se](http://www.mediatryck.lu.se)

**MADE IN SWEDEN** 

*Dedicated to my family*

致我的家人



实事求是

*Seek Truth From Facts*

# Contents

Abstract .....	iii
Popular summary.....	iv
List of publications .....	v
Related works .....	vi
Summary and author contributions.....	vii
Acknowledgments .....	x
<b>1. Introduction .....</b>	<b>1</b>
1.1 Metal-based energy cycle.....	1
1.2 Aluminum as fuel .....	2
1.3 Thesis overview and structure.....	3
<b>2. Aluminum combustion analysis .....</b>	<b>5</b>
2.1 Metal combustion modes .....	5
2.2 Aluminum particle combustion stages .....	7
2.2.1 Ignition .....	7
2.2.2 Symmetric combustion.....	8
2.2.3 Asymmetric combustion.....	8
2.3 Vapor-phase reactions .....	9
2.4 Alumina condensation.....	10
2.5 Emission spectroscopy .....	11
2.5.1 Thermal radiation .....	11
2.5.2 Al spectroscopy .....	14
2.5.3 AlO spectroscopy .....	15
<b>3. Aluminum combustion setups .....</b>	<b>16</b>
3.1 Single droplet combustion.....	16
3.1.1 Setup design and flame conditions .....	16
3.1.2 Burning aluminum droplets .....	18
3.1.3 Burning Al-Mg alloy .....	21
3.2 Aluminum dust flame.....	22
<b>4. Optical diagnostic methods.....</b>	<b>25</b>

4.1 High-speed incandescence-shadowgraph imaging.....	25
4.2 High-speed RGB pyrometry imaging.....	27
4.2.1 Theoretical background .....	27
4.2.2 Calibration .....	28
4.2.3 Optimized RGB pyrometry .....	29
4.3 Spatially-resolved laser absorption spectroscopy of Al atom .....	31
4.3.1 Experimental setup .....	31
4.3.2 Number density determination from SLAS measurements .....	32
4.4 Darkfield and brightfield microscopy .....	33
4.4.1 Optical layout .....	33
4.4.2 Volume and size determination for droplets in the Rayleigh regime .....	35
<b>5. Aluminum combustion characterization .....</b>	<b>38</b>
5.1 Flame structure of single burning aluminum droplets.....	38
5.1.1 From wire ignition to symmetric combustion .....	38
5.1.2 Unsteady combustion .....	40
5.1.3 Theoretical analysis during symmetric combustion .....	42
5.2 Aluminum combustion temperature .....	46
5.2.1 Temperature evolution during wire ignition and combustion ....	46
5.2.2 Temperature evolution during droplet development .....	47
5.2.3 Temperature distribution during symmetric combustion .....	49
5.2.4 Temperature distribution during asymmetric combustion.....	50
5.3 Aluminum atom profile around a burning droplet .....	50
5.4 Nano-oxide formation in the dust flame.....	53
<b>6. Summary and outlook .....</b>	<b>55</b>
6.1 Summary .....	55
6.2 Outlook.....	56
<b>References .....</b>	<b>58</b>

# Abstract

Aluminum is a promising carbon-free energy carrier. The combustion of aluminum in steam offers a novel method for the simultaneous production of hydrogen and heat through the reaction:  $2\text{Al} + 3\text{H}_2\text{O} = \text{Al}_2\text{O}_3 + 3\text{H}_2 + \text{heat}$ . A comprehensive understanding of the combustion mechanism is crucial for predicting and optimizing the performance of aluminum-fueled devices.

This thesis develops different lab-scale aluminum combustion devices and multiple optical diagnostic techniques for flame characterization. Aluminum combustion setups, ranging from single droplets to collective dust flames, are established to provide stable and controllable research targets. The combustion phenomena are inherently complex due to factors such as spatial scales ranging from nanometers to micrometers, transient processes occurring on millisecond timescales, multi-phase dynamics, and extremely high temperatures. To address these challenges, various spatiotemporal diagnostic methods are employed to study key combustion parameters.

A specially designed platform produces single burning aluminum droplets of initial sizes from around 100  $\mu\text{m}$  to 500  $\mu\text{m}$ . The droplets are burning in an adjustable oxidizing environment ranging from an  $\text{H}_2\text{O}/\text{N}_2$  mixture to an  $\text{H}_2\text{O}/\text{N}_2/\text{O}_2$  mixture. The single droplets burning in distinct stages offer unique opportunities for fundamental characterization. Furthermore, a lifted aluminum dust flame is established using aluminum fine powers. This dust flame provides a good target to study flame stabilization, particle-particle interactions, and nano-oxide formation.

Spatiotemporal diagnostic techniques are developed to characterize aluminum flames from different perspectives. First, high-speed incandescence-shadowgraph imaging captures the flame morphology evolution and oxide smoke distribution, simultaneously. The technique determines key parameters, including the flame standoff distance, flame sheet thickness, evaporation rates, and Stefan flow velocity. Second, high-speed RGB pyrometry imaging spatially resolves the surface temperatures of different parts over a burning aluminum droplet and measures the temperature evolution along the wire ignition process and the droplet development process. Then, spatially resolved laser absorption spectroscopy is established to quantify the aluminum atom profile around a burning aluminum droplet. Finally, darkfield and brightfield microscopy quantifies the size and volume of nano-oxide particles in the condensation trail of a jetting aluminum droplet within a dust flame.

With that, the thesis herein contributes key datasets and delivers new knowledge to advance the understanding of aluminum combustion.

## Popular summary

Have you ever imagined burning metals in a power plant instead of fossil fuels like coal? It might sound far-fetched, but metal combustion can turn ordinary metals into potent energy sources. Just think of the brilliant fireworks that light up the festive nights. Those dazzling bursts are only a glimpse of what metal combustion can achieve. But there is much more to the story. Aluminum, for example, releases a tremendous burst of energy when it reacts with oxygen or steam. It is not only the star of pyrotechnics but also a workhorse in applications like solid propellants, underwater propulsion, nanoparticle synthesis, hydrogen production, and thermal spray coating. With its high energy density, abundant reserves, and high reactivity, aluminum emerges as a promising candidate for powering a sustainable future.

In recent years, the vision of a carbon-neutral, green energy cycle based on aluminum has captured growing attention. Imagine a closed-loop system in which burning aluminum produces heat, while the product, aluminum oxide, is recycled using renewable energy like wind or solar to regenerate pure aluminum. In this cycle, aluminum serves as an energy carrier, efficiently transferring renewable energy from regions of surplus to those with high energy demand, all while producing zero carbon emissions. Particularly in a steam-rich environment, aluminum combustion releases half of its energy as heat and harnesses the other half as hydrogen gas, offering dual benefits and vast industrial potential.

To turn the green circle into reality, understanding how aluminum burns is essential. Aluminum combustion typically initiates at the single-particle level, making the study of tiny particle combustion crucial for designing and optimizing large-scale aluminum-fueled applications. This thesis delves into the intricate world of aluminum combustion, focusing on the behavior of micrometer-scale aluminum particles. Although aluminum is solid at room temperature, once ignited, it burns in the vapor phase, leading to complex chemical kinetics. Additionally, the combustion process produces alumina particles ranging from nanometer to micrometer scales through condensation. These fine spatial scales present both challenges and intriguing research opportunities. Moreover, explosive droplet eruptions and fragmentation add complexity to the process, sparking further curiosity about this vigorous phenomenon. These fascinating aspects guide our exploration into the fundamental nature of aluminum combustion.

This thesis develops novel aluminum combustion platforms and employs state-of-the-art optical methods to investigate various aspects of micrometer-scale aluminum droplet combustion, including combustion temperature, flame structure, intermediate species, and nano-oxide formation. We believe that these findings not only deepen the understanding of aluminum droplet combustion dynamics but also provide a robust theoretical foundation for utilizing aluminum as a carbon-free energy carrier in future energy systems.

# List of publications

This thesis is based on the following publications:

- I. **Z. Wu**, C. Ruan, Y. Qiu, M. Stiti, S. Xu, N. Jüngst, E. Berrocal, M. Aldén, X. Bai, Z. Li, Flame structure of single aluminum droplets burning in hot steam flows. *Combustion and Flame*. 271 (2025) 113838.
- II. **Z. Wu**, C. Ruan, M. Stiti, S. Xu, X. Bai, E. Berrocal, M. Aldén, Z. Li, Spatiotemporally resolved surface temperature measurement of aluminum ignition and combustion in steam and oxygenated environments, *Combustion and Flame*. 264 (2024) 113446.
- III. **Z. Wu**, C. Ruan, J. Sun, N. Jüngst, M. Aldén, Z. Li, Visualization of the unsteady combustion of single aluminum droplets: coalescence, eruption, and fragmentation. *Combustion and Flame*. under review.
- IV. C. Ruan, **Z. Wu**, Y. Qiu, E. Berrocal, M. Aldén, X. Bai, Z. Li, Quantitative measurement of aluminum atom number density around a single burning micron-sized aluminum droplet using spatially-resolved laser absorption spectroscopy. *Combustion and Flame*. under review.
- V. C. Ruan, **Z. Wu**, M. Stiti, M. Snellman, Y. Qiu, A. Ahamed Subash, E. Berrocal, M. Aldén, Z. Li, Combustion of micron-sized Al-Mg alloy wires in hot  $\text{H}_2\text{O}/\text{O}_2/\text{N}_2$  flows, *Fuel*. 357 (2024) 129719.
- VI. C. Ruan, **Z. Wu**, J. Sun, N. Jüngst, E. Berrocal, M. Aldén, Z. Li, Ignition, stabilization and particle-particle collision in lifted aluminum particle cloud flames, *Proceedings of the Combustion Institute*. 40 (2024) 105596.
- VII. N. Jüngst; **Z. Wu**, C. Ruan, M. Aldén, Z. Li, Light extinction and scattering to determine nanoparticle formation rates during droplet jetting in aluminum dust flames, *Powder Technology*. (2025) 120633.

## Related works

The following papers are related works but not included in the thesis:

- I. C. Ruan, **Z. Wu**, Y. Qiu, E. Berrocal, M. Aldén, X. Bai, Z. Li, Quantitative measurement of aluminum atom number density around a single burning micron-sized aluminum droplet using spatially-resolved laser absorption spectroscopy. *Combustion and Flame*. under review.
- II. J. Huang, **Z. Wu**, W. Cai, E. Berrocal, M. Aldén, Z. Li, Volume expansion and micro-explosion of combusting iron particles analyzed using magnified holographic imaging, *Powder Technology*. 420 (2023) 118412.
- III. J. Huang, **Z. Wu**, W. Cai, E. Berrocal, M. Aldén, Z. Li, In-situ quantification of spatiotemporally resolved particle concentration in iron powder combustion using holographic imaging, *Powder Technology*. 405 (2022) 117554.
- IV. Y. Qiu, S. Feng, **Z. Wu**, S. Xu, C. Ruan, X. Bai, E.J.K. Nilsson, M. Aldén, Z. Li, Detailed numerical simulation and experiments of a steadily burning micron-sized aluminum droplet in hot steam-dominated flows, *Proceedings of the Combustion Institute*. 40 (2024) 105717.
- V. S. Feng, Y. Qiu, S. Xu, **Z. Wu**, C. Ruan, A. Roth, E. Nilsson, E. Berrocal, Z.S. Li, M. Aldén, X.S. Bai, Modeling of micron-sized aluminum particle combustion in hot gas flow, *Fuel*. 369 (2024) 131718.

# Summary and author contributions

## **Paper I:** Flame structure of single aluminum droplets burning in hot steam flows

This paper introduced an innovative aluminum combustion platform designed to facilitate the controlled combustion of individual aluminum droplets in high-temperature steam flows. Simultaneous high-speed incandescence-shadowgraph imaging was conducted to resolve the transient combustion process with high spatial resolution. The flame structure around the burning aluminum droplets, including flame sheet thickness, flame standoff distance, and droplet evaporation rate, were obtained under different surrounding conditions.

*I designed and optimized the burner. C. Ruan and I designed the wire combustion system. M. Stiti, C. Ruan, E. Berrocal and I planned and conducted the experiments together. I performed all the data analysis and data visualization, and I wrote the manuscript with some input from other co-authors.*

## **Paper II:** Spatiotemporally resolved surface temperature measurement of aluminum ignition and combustion in steam and oxygenated environments

This study presented the spatiotemporal temperature characterization of aluminum wire ignition and particle combustion via high-speed RGB pyrometry. Detailed procedures of particle combustion in symmetric and asymmetric phases were reported in hot  $\text{H}_2\text{O}/\text{N}_2$  and  $\text{H}_2\text{O}/\text{O}_2/\text{N}_2$  flows. Temperature distributions of aluminum droplets at different burning stages were discussed.

*I developed RGB pyrometry with help from Z. Li and M. Stiti. I planned and conducted the experiments with the help from C. Ruan. I performed all the data analysis and data visualization, and I wrote the manuscript with some input from other co-authors.*

## **Paper III:** Visualization of unsteady combustion of single aluminum droplets: coalescence, eruption, and fragmentation

This study unveiled unsteady behaviors in single aluminum droplet combustion with high spatiotemporal resolution. Droplet coalescence, eruption, and fragmentation were resolved by simultaneously capturing flame incandescence and droplet shadowgraphs. The transient surface temperature dynamics of Janus droplets during eruption was reported. Key geometric parameters and criteria for unsteady combustion were identified. The size distribution of nano-oxides during the eruption phase was discussed from ex-situ sample analysis.



*I initiated the study. C. Ruan and I planned and conducted the experiments together. I performed all the data analysis and data visualization, and I wrote the manuscript with some input from other co-authors.*

**Paper IV:** Quantitative measurement of aluminum atom number density around a single burning micron-sized aluminum droplet using spatially-resolved laser absorption spectroscopy

This study introduced a novel optical diagnostic system that combined shadowgraph imaging with spatially resolved laser absorption spectroscopy for detecting aluminum atoms. The technique quantified the concentration of Al atoms around a single micron-sized burning aluminum droplet during the symmetric combustion stage in high-temperature, steam-dominated flows.

*C. Ruan, Z. Li, and I developed the optical diagnostic system. C. Ruan and I planned and conducted the experiments together. I assisted in data analysis on Abel inversion and absorption. I reviewed the paper.*

**Paper V:** Combustion of micron-sized Al-Mg alloy wires in hot  $\text{H}_2\text{O}/\text{O}_2/\text{N}_2$  flows

This paper presented a detailed experimental characterization of the combustion process of micron-sized Al-Mg alloy wires (200  $\mu\text{m}$  diameter) in various hot  $\text{H}_2\text{O}/\text{O}_2/\text{N}_2$  flows using high-speed photography, two-color pyrometry, and spectra measurements. Six oxidizing conditions with varying  $\text{H}_2\text{O}/\text{O}_2/\text{N}_2$  compositions were considered. The morphology and elemental distribution on the surface of the wire after combustion were analyzed with SEM and EDS techniques.

*C. Ruan and I planned and conducted the experiments together. I designed the flame conditions, wrote the experimental method section, and reviewed the paper. I conducted data analysis for two-color pyrometry and spectra measurements.*

**Paper VI:** Ignition, stabilization and particle-particle collision in lifted aluminum particle cloud flames

This study investigated the underlying mechanisms of the ignition, stabilization, and particle-particle collision in lifted aluminum dust flames. High-resolution shadowgraphy and luminosity measurements at a frame rate of up to 50 kHz were implemented to reveal the transient dynamics involved in these processes.

*C. Ruan and I designed and optimized the aluminum dust flame burner together. C. Ruan and I planned and conducted the experiments together. I conducted data analysis on thermocouple temperature correction and aluminum size statistics. I reviewed the paper.*

**Paper VII:** Light extinction and scattering to determine nanoparticle formation rates during droplet jetting in aluminum dust flames

This study investigated the light extinction and scattering of aluminum dust flame via high-speed darkfield and brightfield microscopy. We elaborated an approach to two-dimensionally measure the instantaneous volume and size of alumina nanoparticles produced during single droplet jetting in the dust flame.

*N. Jüngst, C. Ruan, and I conducted experiments together. I was actively involved in the discussion regarding data analysis, result interpretation, and manuscript preparation. I reviewed the paper.*

# Acknowledgments

Time races by. This journey now draws to a close. I am very fortunate to have met so many wonderful colleagues and friends along the way. This thesis would not have been possible without your support, encouragement, and companionship. I am truly grateful.

First, I would like to express my gratitude to my main supervisor, *Zhongshan Li*, who has been by my side throughout the past four years. Your office is always open to me, and our countless discussions on work, research, and life have been invaluable to my growth. You have continuously inspired me and challenged me to improve my work. Your expertise, dedication, and approach to research have been guiding me to become an independent researcher.

I would also like to thank all my co-supervisors. First, my sincere thanks to *Marcus Aldén* for giving me the opportunity to join this incredible division. I am especially grateful for your active involvement in the metal project and your sharp questions and inspiring suggestions during our many metal meetings. Next, a big thank you to *Arman Ahamed Subash*. Starting a lab from scratch was challenging, and your assistance with lab construction and guidance on experimental safety was indispensable. Your continual support and encouragement have meant a great deal to me. Also, I extend my deep gratitude to *Christian Brackmann*. You are always ready to help whenever problems arise in the lab. Your careful, reliable, and responsible attitude has been both inspiring and impressive. I feel so fortunate to have you around.

Many thanks to all my collaborators. First, to *Can Ruan*. You joined the metal project a year and a half after I did, and since then, your contributions have significantly boosted our experimental efforts and project progress. I will never forget the days and nights we spent together in the lab. You are a reliable teammate, and I am grateful for all your contributions. To *Yue Qiu*. We joined the metal project together. Over the years, we have shared our knowledge and perspectives to overcome the research challenges. Thank you for the many fruitful discussions and unwavering support that have enriched the work. To *Edouard Berrocal*. I would like to express my deep gratitude for your assistance with optical imaging and lab construction. You have invested so much time in the lab and have taught me a lot about conducting a good experiment. I appreciate your invaluable contributions. To *Xue-Song Bai*. Every time I bring questions to your office, you can always clarify my doubts and offer valuable suggestions. I am deeply grateful for your expertise, warmth, and kindness. To *Mehdi Stiti*. Your guidance and help with the optical measurements meant a great deal to me. Thank you for your support. To *Niklas Jüngst*. Working with you over the past year has been a pleasant experience. I am grateful for your efforts and support. To *Jinguo Sun*. You have been a reliable friend whenever I face any problems. Thank you for your strong support. To *Shijie Xu*. I

extend my gratitude for all the modeling support and theoretical expertise you provided. To *David Andersson*. Thanks for all the discussions and the efforts together in the lab. FRAME with Aluminum Combustion has been quite exciting.

Many thanks also to the current and previous division leadership, *Joakim Bood*, *Per-Erik Bengtsson*, and *Marcus Aldén*, thanks for your contributions in organizing such a unique and wonderful institute. I am deeply grateful to the administrative team, *Minna Ramkull*, *Cecilia Bille*, *Igor Buzuk*, *Charlotta Åberg*, *Ida Scherman*, *Elizabeth Zhang*, and *Emelie Niléhn*. Your strong support makes this division a truly pleasant place to work. I also extend my sincere thanks to *Sven-Inge Möller* for all the support and encouragement. Many thanks also to all the colleagues and friends at Combustion Physics for contributing to such an amazing working environment. You make this journey much easier.

Special thanks to *Anna-Lena Sahlberg*, *Thi Kim Cuong Le*, *Andreas Ehn*, and *Zhongshan Li* for providing me with valuable teaching opportunities. I also extend my gratitude to my teaching colleagues, *Sabrina M. Gericke*, *Aravind Sridhara*, *Yue Qiu*, *Meena Raveesh*, and *Alsu Zubairova*. I have learned a lot and truly cherished the experience.

I would also like to thank my officemate, *Saga Bergqvist*. Our many discussions and shared laughs have been invaluable, and I truly appreciate your help, support, and all the lovely gifts. I am so lucky to have you as my officemate and friend. My sincere thanks also go to the Trivselgruppen teammates, *Adrian Roth*, *David Sanned*, *Yue Qiu*, *Sabrina M. Gericke*, and *Lisa Rämisch*. Your passion and creativity bring so much joy to the division. I am very happy to be a part of it.

Special thanks to the “Fire Gang”, *Michael*, *Thommie*, *Shijie*, and *Morteza*. Our many trips together over the years have added so much fun to my life in Sweden. “Do more!” Thanks also to the Chinese friends at Combustion Physics, *Xin Liu*, *Qingshuang Fan*, *Yupan Bao*, *Kailun Zhang*, *Ruike Bi*, *Jundie Chen*, *Jianqing Huang*, *Weitian Wang*, and *Xiaomin Ni*, for all your help and support. Thanks to *Huaiyu Chen* for guiding me on a fantastic visit to MAX IV. Many thanks also to the friends from M building, *Leilei Xu*, *Miao Yang*, *Xiufei Li* and *Yuxiang Lim*, for your company. I also appreciate the basketball friends from EOS, *Alan*, *Xin*, *Dong*, *Huafei*, *Yihuai*, and *Jiangong*, as playing together always helps ease work fatigue.

I would also like to thank the financial support from the *Knut and Alice Wallenberg Foundation*, which made it possible for me to carry out the research.

Finally, I would like to thank *my family*, especially *my parents and my sister*, for their endless support and love. 亲爱的父亲、母亲和姐姐，感激你们无条件的无私奉献和坚定支持，你们的爱是我前进的最大动力。亲爱的亲人们，衷心感谢你们从小到大给予我的温暖关怀，你们的支持对我无比重要。I would also like to thank *Xinrui* for your steadfast companionship over the years. Your love and support have meant a great deal to me.



# 1. Introduction

## 1.1 Metal-based energy cycle

Global concerns over climate change and energy shortage have intensified the need to transition from fossil-based energy systems to renewable energy solutions [1,2]. The ongoing energy transition is marked by increased electrification and a significant rise in power generation from renewable sources, particularly solar and wind, which hold the greatest potential for renewable electricity production [3]. However, the inherent fluctuations in electricity generation from these sources create a temporal mismatch between supply and demand [4]. To address this, sustainable solutions for storing and transporting renewable electricity are essential to bridge the spatial and temporal gaps between availability and demand.

An innovative carbon-free metal-based solution has recently been proposed [5–9], as depicted in Figure 1.1. This concept utilizes metals, such as aluminum or iron, as energy carriers in a sustainable energy cycle. In the storage phase, renewable electrical energy is chemically stored in metals via direct electrochemical or thermochemical reduction using green hydrogen [10,11]. These metals can be transported to regions with energy demand. In the release phase, the stored energy

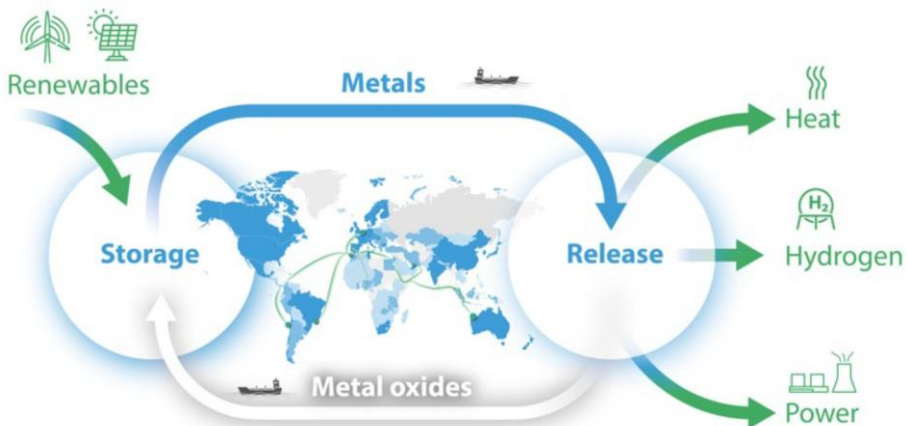


**Figure 1.1:** A schematic of the metal-based clean energy cycle. Figure adapted from [9].

is recovered through combustion or low-temperature oxidation, generating heat and/or hydrogen. The produced metal oxides, typically solid under standard conditions, can be collected and reduced back to pure metals, thereby completing an energy cycle.

Metal fuels offer significant advantages as globally carbon-free energy commodities. First, metals provide high energy densities, as shown in Figure 1.2, which compares the energy density and specific energy of various metals (Al, Fe, Mg, B, Si) with fossil fuels and other carbon-free fuels ( $H_2$  and  $NH_3$ ). This high energy density underscores their potential as viable fuels. Additionally, metals are carbon-free, permit safe storage with minimal loss, and enable secure long-distance transportation. They are abundant, recyclable, and potentially adaptable to various energy demands, from stationary power generation to portable vehicle engines.

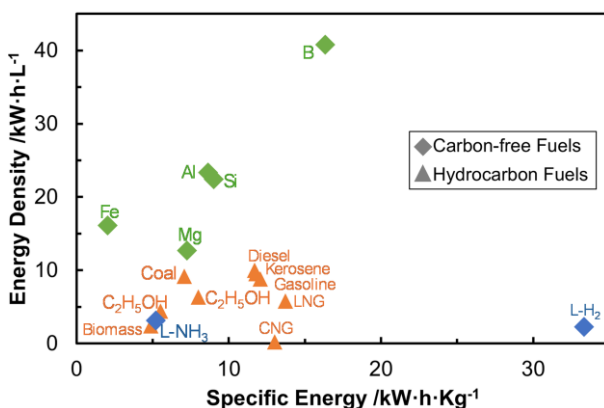
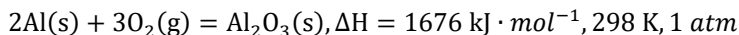
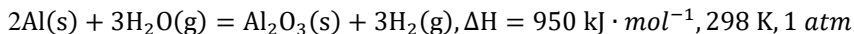


**Figure 1.2:** Specific energy and energy density of common fuels. Data sources: [5,12,13].

## 1.2 Aluminum as fuel

Aluminum (Al) is regarded as one of the most promising energy carriers [10,14,15]. It is the most abundant metal and the third most abundant element in the crust of the earth, comprising approximately 8% by mass [16]. Over bulk aluminum, a thin dense oxide layer naturally forms on the surface upon exposure to air and other oxidizers. This passivating layer, only a few nanometers thick, blocks the material from further oxidation under ambient conditions, preventing energy loss and ensuring safe long-term storage and transportation. Additionally, aluminum is highly reactive and can burn in various oxidizers, including  $O_2$ ,  $H_2O$ ,  $CO_2$ , and  $N_2O$ . In the past, aluminum powders have been utilized as fuel additives in pyrotechnics [17,18], solid propellants [19,20], explosives[21,22], and underwater propulsion

systems [23,24]. Aluminum combustion can occur in steam (H<sub>2</sub>O), releasing heat and hydrogen, or in oxygen (O<sub>2</sub>), releasing heat, according to the reactions below.



In the context of a clean energy cycle, the combustion of aluminum in high-temperature high-pressure steam, in particular, offers an efficient method for simultaneously producing high-quality heat and hydrogen, without generating pollutants [25,26]. Recently, Halter et al. [27] experimentally demonstrated the co-generation of heat and hydrogen by high-temperature oxidation of aluminum powders in steam. It provided empirical support for this energy concept. When aluminum burns in steam, approximately half of its chemical energy is released as heat, while the other half is stored in H<sub>2</sub>, which can be used in fuel cells, turbines, or heat engines. Therefore, the Al-H<sub>2</sub>O combustion enables in-situ hydrogen production, offering a convenient solution for hydrogen supply while eliminating the safety concerns associated with large-scale hydrogen storage and transportation. Additionally, direct Al-air combustion is a promising approach to maximize power density. The approach offers alternative way for using aluminum as a fuel to meet diverse power requirements.

## 1.3 Thesis overview and structure

The primary aim of this thesis is to advance our fundamental understanding of aluminum droplet combustion. To this end, various laboratory-scale aluminum combustion setups have been established, ranging from single-droplet combustion to collective powder dust burning under different conditions. Accordingly, advanced optical diagnostic techniques have been developed to characterize key aspects of the flames, including flame structure, combustion temperature, nano-oxide formation, and intermediate species. These techniques offer in-situ characterization with high spatiotemporal resolution, providing new insights into the complex burning phenomena.

The thesis is structured as follows:

**Chapter 2** introduces the general knowledge of aluminum particle combustion and highlights several key research questions.

**Chapter 3** details the development of lab-scale aluminum flames, including the experimental setups and flame conditions, which serve as the primary targets for investigation.



**Chapter 4** describes the various optical diagnostic methods developed for aluminum flame characterization, covering the principles, experimental setups, and data analysis.

**Chapter 5** presents the experimental highlights and key findings of this thesis.

**Chapter 6** summarizes the present work and elaborates on future research.

## 2. Aluminum combustion analysis

In this chapter, the fundamental background of aluminum combustion is introduced. Metal particles can combust in different modes depending on the physical-chemical properties of the particles and the oxidizing environments. Typical combustion stages for micrometer aluminum particles are introduced. Some key aspects of aluminum combustion, including gas-phase kinetics, alumina condensation, and aluminum flame spectroscopy are discussed.

### 2.1 Metal combustion modes

Metal fuels exhibit distinctive combustion characteristics compared to traditional hydrocarbon fuels. For liquid hydrocarbons, the droplet flame temperature significantly exceeds the boiling point of the fuel, enabling vapor-phase combustion as the fuel vaporizes and diffuses toward the oxidizer. In contrast, metals have much higher boiling points, fundamentally altering their combustion behavior. According to Glassman's criterion [28], a metal must have a flame temperature exceeding its boiling point to undergo vapor-phase combustion. The flame temperature is often limited by the vaporization-dissociation point of the condensed metal oxide. This is because the heat of vaporization-dissociation of the metal oxide is higher than the heat available to raise the condensed state of the oxide above its boiling point [28].

The description of metal combustion modes typically starts with single, isolated metal particles. For particles burning in oxygen, combustion modes are classified based on how the metal is oxidized to its initial suboxides. This oxidation can occur either homogeneously via vapor-phase reactions or heterogeneously via surface reactions. Based on these criteria, metal combustion can be categorized into three modes [29]:

- A. Vapor-phase combustion of the evaporated metal.
- B. Heterogenous combustion forms volatile oxides or suboxides.
- C. Heterogenous combustion forms non-volatile oxide that dissolves in the metal droplet.

For a metal whose flame temperature is higher than its boiling point, combustion occurs in the vapor phase, referred to as mode A in Figure 2.1. In this case, the metal

particles are heated to their boiling point, causing the metal vapor to diffuse outward and react with the oxidizer, forming a diffusion flame around the droplet. If the flame temperature is below the boiling point of the metal, combustion occurs through heterogeneous multi-phase surface reactions. This process can proceed in two distinct modes. In mode B in Figure 2.1, the combustion heat is sufficient to vaporize the metal oxides, leading to the formation of gaseous metal oxides/suboxides on the metal surface, which then diffuse away and condense in the condensation zone. In contrast, if the combustion heat is insufficient to vaporize either the metal or its oxides, the combustion follows mode C in Figure 2.1, where liquid oxide forms on the metal surface. The physical properties of aluminum, boron, and iron, along with their burning temperature in air, are listed in Table 2.1. According to this classification, aluminum, boron, and iron represent typical examples of metals that combust in modes A, B, and C, respectively.

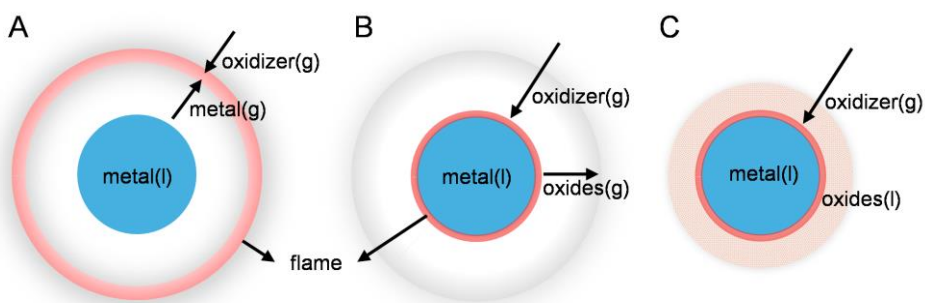


**Figure 2.1:** Combustion modes of metals. Figure reproduced from ref. [5].

**Table 2.1:** Physical properties of aluminum, iron, bone, and their oxides, as well as the combustion modes.

Metals and oxides	Melting point /K	Boiling Point /K	Burning temperature (condensed phase) in air /K	Combustion mode
Aluminum (Al)	933	2790	~3400 [30,31]	A
Alumina ( $\text{Al}_2\text{O}_3$ )	2327	~4000		
Boron (B)	2450	3931	~3000 [32,33]	B
Boron oxide ( $\text{B}_2\text{O}_3$ )	723	2316		
Iron (Fe)	1811	3135	~2500 [34,35]	C
Iron oxide ( $\text{Fe}_2\text{O}_3$ )	1838	2896		

## 2.2 Aluminum particle combustion stages

Aluminum is one of the most promising metal fuels. Intensive experimental and theoretical investigations on aluminum combustion have been conducted during the past decades. However, obtaining a complete understanding of aluminum combustion has been challenging, due to multiple reasons: (1) combustion occurs on a micrometric scale within milliseconds under very high temperatures, (2) combustion varies significantly over experimental conditions (oxidizers, temperature, etc.), (3) a wide variety of experimental methods have been employed, resulting in substantially scattered experimental results. Based on available studies, an overview of the particle combustion process is briefly discussed. For a single micrometer aluminum particle burning in oxidizers ( $\text{O}_2$ ,  $\text{H}_2\text{O}$ ,  $\text{CO}_2$ ,  $\text{N}_2\text{O}$ ), the particle follows distinct combustion stages as depicted in Figure 2.2: (I) raw aluminum particle, (II) ignition, (III) symmetric combustion, and (IV) asymmetric combustion.

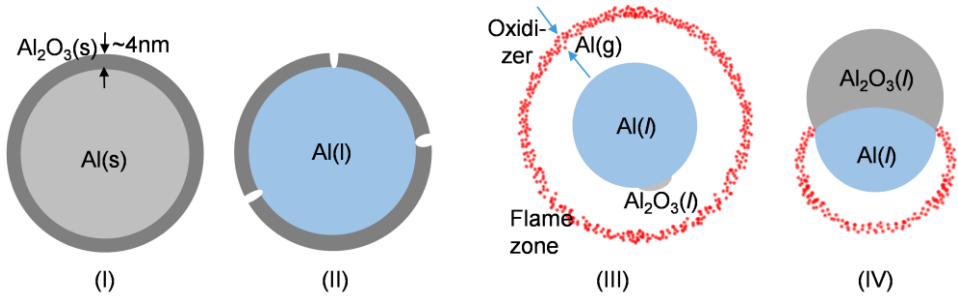


**Figure 2.2:** Typical burning stages of micrometer aluminum particles.

### 2.2.1 Ignition

Raw aluminum particles are typically covered by a stiff alumina layer of approximately 4 nm thick. Aluminum ignition is triggered by the rupture of this oxide layer. Sundaram et al. [36] summarized the ignition temperature for particles of various sizes. They suggest that the ignition temperature decreases with decreasing particle size, from about 2330 K at 100  $\mu\text{m}$  to about 1000 K at 100 nm. Initially, the aluminum particle is heated to the melting point of the aluminum core (933 K). As the core temperature increases, its volume expands by about 11% due to the reduction in aluminum density, creating tensile stress that fractures the oxide layer. These fractures expose the aluminum core to oxidizers, allowing oxidation to occur. The heat released during this oxidation can ignite nanometer particles. However, in micrometer particles, the heat generated is insufficient due to their higher volumetric heat capacity. These larger particles must instead be heated to the melting point of the alumina layer (2327 K) to achieve ignition.

Due to the inert oxide layer, igniting aluminum is not a straightforward task in experimental practice. For single-particle combustion, most studies employ high-power lasers [37–42], hydrocarbon flames [43–45], or plasma discharge [46,47]. These ignition facilities introduce additional complexities to the overall combustion system. The challenges in igniting individual aluminum particles also complicate the ignition and stabilization of aluminum dust flames. Thus, one of the major tasks of this work is to develop stable and repeatable aluminum combustion to facilitate advanced optical measurements.

### **2.2.2 Symmetric combustion**

After ignition, the molten alumina shrinks into a small cap attached to the aluminum droplet surface, leaving the majority of the surface exposed to the surrounding oxidizers. Aluminum vaporizes from the surface and contacts the oxidizers, forming a diffusion flame encapsulating the droplet core, as shown in Figure 2.2(III). A large amount of hot condensed alumina products form in the flame region. The heat from the flame is conducted back to the surface to sustain evaporation. The droplets maintain a quasi-steady combustion state. During this stage, the small oxide cap has a negligible effect on the distribution of aluminum vapor velocity profile.

The symmetric stage represents an important process for understanding the fundamentals of aluminum combustion [48]. Key parameters during this stage, such as combustion temperature (temperature of aluminum and alumina), aluminum evaporation rates, flame standoff distance, intermediate species distribution, and oxide condensation, are significant for the build-up and validation of a reliable combustion model. For instance, during symmetric combustion, temperatures of different parts within the burning droplet, including the aluminum core, the condensed alumina product, and the gas-phase species between the droplet and flame front, are to be quantitatively evaluated. The structurally resolved temperature of the burning droplet is essential to get a full picture of the droplet combustion. Besides, aluminum droplets keep evaporating during combustion and the size change of the droplet is important for evaluating the heat and mass transfer rates between the flame and the aluminum droplet. However, experimental determination of these parameters requires spatiotemporal diagnostics combined with proper combustion targets, which have been challenging to achieve within the metal research community, and only a few groups have provided such results. One of the highlights of this thesis is the detailed, spatially resolved characterization of the aluminum droplet combustion.

### **2.2.3 Asymmetric combustion**

Asymmetric combustion is an intrinsic and unique characteristic of aluminum combustion. At the end of the symmetric combustion phase, the oxide cap grows as

the alumina smoke coalesces with the central aluminum core. The resulting droplet consists of two immiscible components, liquid aluminum, and alumina, with comparable volumes, described as a ‘Janus’ droplet. Combustion then transits to an asymmetric mode, where the flame front envelops the aluminum portion, while the alumina cap remains exposed to the surrounding environment, as illustrated in Figure 2.2(IV). Note that the emissivity in the visible range of molten alumina is typically several (3-5) times higher than the pure liquid aluminum at the same temperature [49,50], thus the alumina side is brighter than the aluminum side, which helps to distinguish the structure evolution. During the asymmetric stage, the oxide cap keeps growing due to oxide coalescence, which is a key feature. Gallier et al. [51] proposed that thermophoresis is an effective mechanism driving the oxide smoke back to the aluminum surface, hence a major contributor to cap development. During this process, in addition to the heat feedback from the flame, the accumulation of hot oxides also provides heat for aluminum evaporation through thermal conduction.

The oxide cap plays a predominant role in shaping the burning behavior [52]. Compared to the symmetric stage when the effect of the cap can be neglected, the cap in this stage covers a larger portion of the aluminum surface, which stops aluminum evaporation from the covered region. Thus, it distorts the profile of aluminum evaporation velocity, temperature, alumina production, and other quantities around the droplet. Moreover, the oxide cap also contributes to unsteady combustion, such as droplet eruption and fragmentation, commonly occurring at the end of the burning process [53]. Overall, the existence of the oxide cap can lead to complex unsteady combustion behaviors.

Key aspects in this stage include oxide cap evolution, unsteady combustion behaviors, and temperature variation. For instance, how the cap evolves will directly determine the structure of the Janus droplet that decides the area of evaporation from the exposed aluminum. The cap growth rate also accounts for the heat conduction rate from cap to aluminum that supports its evaporation. Additionally, unsteady burning behaviors, like eruption and fragmentation, are significant features that affect the combustion rate and product size distribution. Detailed characterization of these behaviors are desirable, which call for spatiotemporally resolved experimental investigations.

## 2.3 Vapor-phase reactions

Vapor-phase reactions dominate the aluminum combustion process [54]. Therefore, the gas-phase chemical mechanism plays a significant role in the prediction of the combustion process. Several kinetic models have been proposed for the Al/O/C/H system [55–58]. For example, Huang et al. [56] presented an aluminum-containing

sub-mechanism consisting of 15 species and 22 reactions. For the gaseous aluminum-steam system, two reactions of the Al atoms and H<sub>2</sub>O molecules are considered as the principal chain initiation channels: (1)  $\text{Al} + \text{H}_2\text{O} = \text{AlO} + \text{H}_2$ , and (2)  $\text{Al} + \text{H}_2\text{O} = \text{AlOH} + \text{H}$ . They suggested that the rate constant of the channel (1) is much higher than that of the channel (2). The dominant oxidation pathway for the Al-H<sub>2</sub>O reaction system is presented in Figure 2.3. In this system, H<sub>2</sub>O molecules dissociate or react with Al species and produce H and OH, but not significant amounts of O atoms. In the Al-O<sub>2</sub> system, O<sub>2</sub> molecules can dissociate or directly react with Al following the chain initiation reaction  $\text{Al} + \text{O}_2 = \text{AlO} + \text{O}$ . This process generates a large amount of O atoms which help to accelerate the formation of Al<sub>2</sub>O<sub>3</sub>. This explains why the burning rate is much slower when aluminum burns in steam than in oxygen [59,60].



**Figure 2.3:** Dominant reaction pathways for the gaseous aluminum-steam reaction system. Figure reproduced from ref. [56].

However, large uncertainties still exist on the reaction rate constants and key reaction pathways. Further optimizations require more theoretical analysis and experimental investigations. Some key species, such as Al, AlO, and AlOH, are generally recognized by most of the models, which motivates experimental efforts in the investigation of these species. For example, Bucher et al. [41,42] conducted Planar laser-induced fluorescence (PLIF) to map out the AlO distribution and the AlO gas-phase vibrational temperature field in the flame envelope of individual droplets burning different oxidizers. Besides, Vilmart et al. [61] detected the Al atom in a solid-propellant flame using Al-PLIF. Similar laser-based explorations for the quantitative determination of the key species can provide valuable data for optimizing the kinetic models.

## 2.4 Alumina condensation

Another feature of aluminum combustion is the formation of condensed-phase alumina. Theoretical studies [62–65] have stressed that alumina condensation contributes a large amount of heat release that can be comparable to the heat release from chemical reactions. It emphasizes the significant role of oxide condensation in aluminum combustion.

The formation of alumina aerosol particles mainly follows three processes: (1) homogeneous nucleation, (2) condensational growth, and (3) coagulation. Homogeneous nucleation from gaseous  $\text{Al}_2\text{O}_3$  is the predominant process during the initial combustion stage, followed by alumina droplet growth mainly in two ways: either by condensation of  $\text{Al}_2\text{O}_3(\text{g})$  molecules on the previously formed alumina droplets, or by heterogeneous reactions on the droplet surface involving aluminum sub-oxides, i.e.,  $\text{AlO}$ ,  $\text{AlO}_2$ ,  $\text{Al}_2\text{O}_2$ , etc., and atomic oxygen. Meanwhile, coagulation happens due to Brownian motion or turbulence leading to larger droplets. Due to the modeling complexity, several models [52,66,67] simplified their condensation models as a pure homogeneous nucleation process, and only a few studies [63,65] have taken the whole three stages into account.

A complete understanding of the condensation mechanism is crucial for predicting and controlling the product size distribution and heat release rate. Condensed alumina particles generally range from nano-to-micrometer scale. Detailed in-situ quantification of alumina particle formation relies on advanced microscopic optical diagnostic techniques. On the other hand, since condensation significantly contributes to the heat released during combustion, the condensed alumina droplets typically possess high temperatures. The majority of heat transfer from aluminum combustion to the surrounding environment occurs through thermal radiation emitted by these hot alumina droplets [68]. Therefore, knowledge of the radiative properties of nano-to-micrometer alumina droplets is critical in estimating the radiative power of an aluminum flame.

## 2.5 Emission spectroscopy

Aluminum flames, either a flame around a single particle or an aluminum dust flame, are characterized by their intense luminosity. A flame is shown in Figure 2.4(a). The corresponding emission spectra, shown in Figure 2.4(b), featured three main components associated with aluminum: (1) continuum thermal radiation extending from infrared to near-ultraviolet, (2) aluminum monoxide ( $\text{AlO}$ ) molecular bands primarily in the  $\sim 460\text{--}520\text{ nm}$  range, and (3) atomic aluminum ( $\text{Al}$ ) lines centered at around  $394\text{ nm}$  and  $396\text{ nm}$ .

### 2.5.1 Thermal radiation

The intense luminosity mainly arises from the thermal radiation of condensed-phase emitters within the flame, including hot aluminum droplets and alumina products. Notably, numerous alumina droplets in nano-to-micrometer scale, are produced at temperatures exceeding  $3000\text{ K}$  [69–71]. These high-temperature emitters generate strong incandescence via thermal radiation.



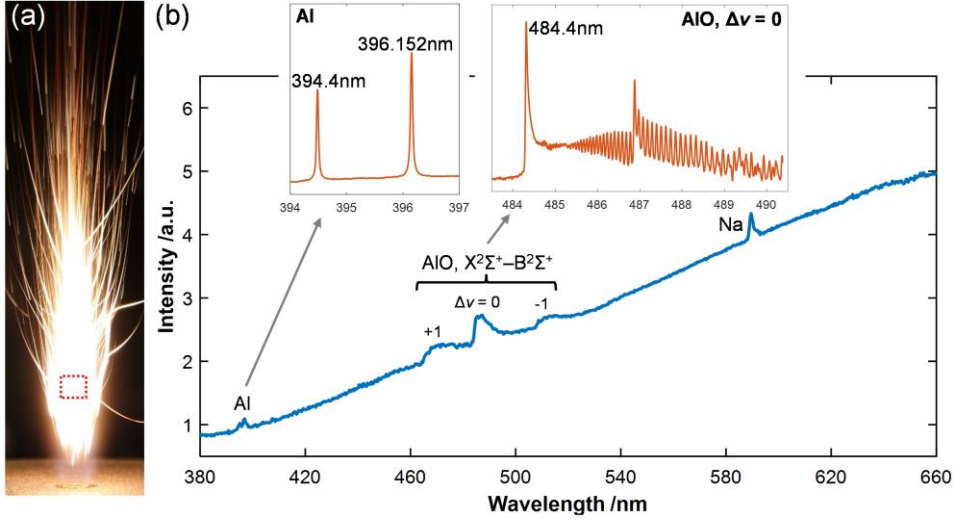


**Figure 2.4:** (a) Aluminum dust flame. The red dashed box indicates the region where the spectra are taken. (b) The flame spectra, as well as the Al atomic lines and the AIO emissions.

### 2.5.1.1 Blackbody radiation

The radiation energy emitted by a blackbody per unit time and unit surface area is proportional to the fourth power of the absolute temperature, which is described by the Stefan–Boltzmann law [72] in Eq. (2.1):

$$I_b = \sigma T^4 \quad (2.1)$$

where  $I_b$  is the total blackbody radiance,  $\sigma$  is the Stefan–Boltzmann constant, and  $T$  is the absolute temperature of the surface in K. The spectral blackbody radiance  $I_{b,\lambda}$  is described by Planck’s law in Eq. (2.2), which quantifies the amount of radiation energy about the wavelength  $\lambda$  emitted by a blackbody at a temperature of  $T$  per unit time, per unit surface area, and per unit wavelength.

$$I_{b,\lambda}(\lambda, T) = \varepsilon(\lambda, T) \frac{2\pi h c^2}{\lambda^5 (e^{\frac{hc}{\lambda k T}} - 1)} \quad (2.2)$$

where  $\varepsilon(\lambda, T)$  denotes the emissivity that is one for a blackbody.  $c$  is the speed of light,  $h$  is Planck’s constant, and  $k$  is the Boltzmann constant.

The wavelength dependence of the spectral blackbody radiance is plotted in Figure 2.5. Thermal radiation is a continuous function of wavelength. At a certain temperature, the radiation increases with wavelength, reaches a peak, and then decreases with wavelength. At any wavelength, the amount of emitted radiation increases with increasing temperature. As the temperature increases, the peak of the

curve shifts toward shorter wavelengths. The peak wavelength for a specified temperature is given by Wien's displacement law in Eq. (2.3):

$$\lambda_{\max} = \frac{2897.8}{T} \mu\text{m} \quad (2.3)$$

Planck's law is the theoretical foundation for surface temperature measurements using multi-spectral pyrometry, which is introduced in Section 4.2.

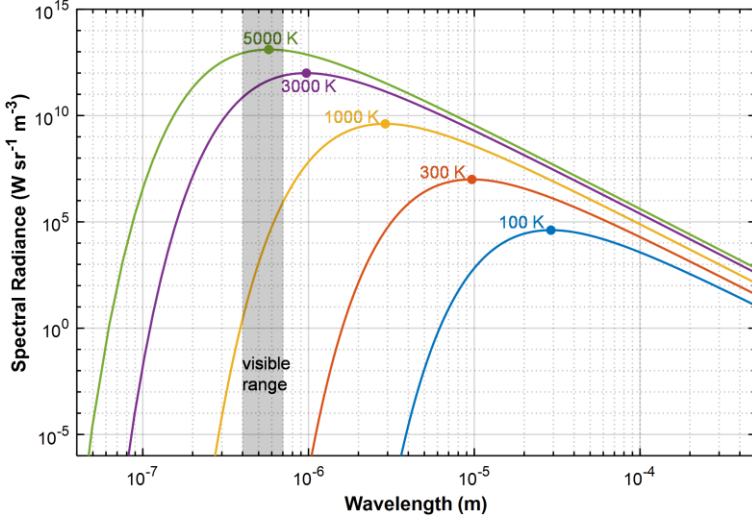


**Figure 2.5:** The variation of the blackbody radiance with wavelength at temperatures from 100 K to 5000 K. The dot on each curve marks the peak.

#### 2.5.1.2 The emissivity of alumina

The emissivity  $\varepsilon(\lambda, T)$  is the ratio of radiation emitted by a surface to that emitted by a blackbody at the same temperature. It varies between zero and one ( $0 \leq \varepsilon \leq 1$ ), with  $\varepsilon = 1$  indicating a perfect blackbody. Emissivity serves as a measure of how closely a real surface behaves like a blackbody and varies with both temperature and wavelength. When the emissivity is independent of wavelength, the surface is referred to as a graybody. Since alumina oxides are the major source of the continuum radiation in an aluminum flame, understanding the emissivity of alumina oxides is essential for accurately determining aluminum flame temperature.

So far, the emissivity of alumina particles remains unclear, especially in nano-to-micrometer scale [73]. Assumptions about the spectral dependence of alumina emissivity vary widely, from graybody behavior to  $\lambda^n$  dependence, where  $n$  is commonly -1 or -2. For instance, Poletaev and Florko [74] suggested that the spectral emissivity of aluminum dust flames is wavelength-independent. In contrast, Goroshin et al. [31] reported that the spectral emissivity of aluminum flames scales

as  $\lambda^{-2}$ . Few studies reported the measurements on the emissivity of alumina particles. Lynch et al. [50] found that the micrometer alumina particle could be approximated as a graybody at high temperatures (3000–3300 K), while nanometer particles exhibited a wavelength dependence of  $\lambda^{-1.4}$  at 2824 K. Using a similar setup, Kalman et al. [75] observed that the emissivity of optically thin micrometer alumina particles followed a  $\lambda^{-1.4}$  dependence in the 2800–3500 K range, whereas nanoscale alumina particles displayed a weaker wavelength dependence of  $\lambda^{-1.2}$ . Overall, nanometer scale alumina particles (typically  $\sim 100$  nm), being smaller than the wavelength of light, exhibit strong wavelength-dependent emissivity. In contrast, micrometer scale alumina particles tend to approximate graybody behavior, especially at high temperatures.

### 2.5.2 Al spectroscopy

One of the key features of the aluminum flame spectra is aluminum atomic lines centered at 394.4 nm and 396.152 nm. The two lines originate from the  $^2S_{1/2} \rightarrow ^2P_{1/2}$  and  $^2S_{1/2} \rightarrow ^2P_{3/2}$  transitions, respectively.

A neutral aluminum atom has a ground-state electron configuration in  $3S^23P$ , where one unpaired electron is beyond a closed shell. The ground term  $^2P$  is split by fine structures in two sublevels:  $^2P_{1/2}$  and  $^2P_{3/2}$ .  $^2P_{1/2}$  is the absolute ground-state and  $^2P_{3/2}$  is a slightly higher sublevel ( $112 \text{ cm}^{-1}$  above the absolute ground) [76], as illustrated in Figure 2.6. Relative populations of the aluminum atoms at the two levels are estimated by a Boltzmann distribution [77]:

$$\frac{n_1}{n_2} = \frac{g_1}{g_2} \exp\left(\frac{E_2 - E_1}{\kappa T}\right) \quad (2.4)$$

where the subscripts 1 and 2 indicate the  $^2P_{1/2}$  and  $^2P_{3/2}$  state, respectively.  $n$  represents the populations of Al atoms,  $T$  is the temperature,  $E$  denotes the energy levels, and  $g$  is the degeneracy of the two states.

In an aluminum flame, the aluminum atoms are excited from its ground configuration  $3S^23P$  to  $3S^24S$ . More specifically, the transition populates the excited state with the term symbol  $^2S_{1/2}$ . Once populated, those excited aluminum atoms relax via electric dipole transitions back to ground level, as illustrated in Figure 2.6. The transitions produce the lines shown in Figure 2.4. The spectroscopic data of the two transitions are listed in Table 2.2. The theory provides the fundamental background for the experiments of laser absorption spectroscopy of the Al atom, which will be introduced in Section 4.3.

**Table 2.2** The spectroscopic data of the two transitions

Transition k → i	$\lambda$ /nm	$A_{ki}$ / $10^8\text{s}^{-1}$	$E_k$ /cm <sup>-1</sup>	$E_i$ /cm <sup>-1</sup>	$g_k$	$g_i$
$^2S_{1/2} \rightarrow ^2P_{1/2}$	394.4	0.498	25347.756	0.000	2	2
$^2S_{1/2} \rightarrow ^2P_{3/2}$	396.152	0.982	25347.756	112.061	2	4

$\lambda$ : wavelength,  $A$ : Einstein coefficients,  $E$ : energy level,  $g$ : degeneracy

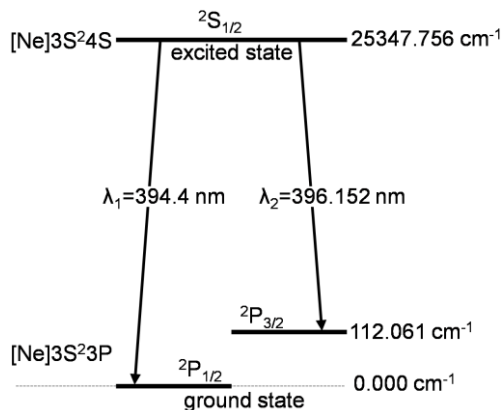


**Figure 2.6:** Transitions of the aluminum atoms: (1)  $^2S_{1/2} \rightarrow ^2P_{1/2}$  at 394.4 nm, (2)  $^2S_{1/2} \rightarrow ^2P_{3/2}$  at 396.152 nm.

### 2.5.3 AlO spectroscopy

Another key feature of the flame spectra is the AlO bands in the blue-green region, which originates from the  $X^2\Sigma^+ - B^2\Sigma^+$  molecular transitions. AlO is a diatomic radical with several low-lying electronic states, the most important of which for spectroscopic studies are labeled  $X^2\Sigma^+$ ,  $A^2\Pi^+$ , and  $B^2\Sigma^+$  [78]. The commonly observed electronic transition is from the ground state  $X^2\Sigma^+$  to the excited state  $B^2\Sigma^+$ . The three most intense bands within the electronic transition come from the vibrational transitions:  $\Delta v = 0, -1$ , and  $+1$ , as shown in Figure 2.4. Several studies [31,79,80] derived the aluminum flame temperature by fitting the spectral shape of the AlO  $\Delta v = -1$  molecular band, due to the sensitivity of its shape to the temperature over the range encountered in aluminum combustion.

# 3. Aluminum combustion setups

Two combustion setups were designed to study aluminum combustion in different forms: (1) single droplet combustion, and (2) dust flame.

## 3.1 Single droplet combustion

### 3.1.1 Setup design and flame conditions

The setup consists of a modified porous plug burner with central jets and a positioning device for aluminum wires, as shown schematically in Figure 3.1(a). The aluminum wire is held by two horizontally arranged ceramic tubes and is automatically positioned above the central outlet of a burner at a height of 4 mm by a rotation stage. The stage can send out TTL signals for synchronization of measurement devices. Figure 3.1(b) presents a flat flame burner [81] that is modified to provide an oxidizing environment for aluminum ignition and combustion. Two concentric tubes in the center of the burner are used to form an  $\text{H}_2/\text{O}_2$  diffusion flame. The inner diameters of the  $\text{H}_2$  and  $\text{O}_2$  tubes are 1.5 and 5.0 mm, respectively. The diffusion flame heats the aluminum wire to its ignition temperature (melting point of alumina, 2327 K). A premixed  $\text{H}_2/\text{O}_2/\text{N}_2$  flat flame provides a hot co-flow in the

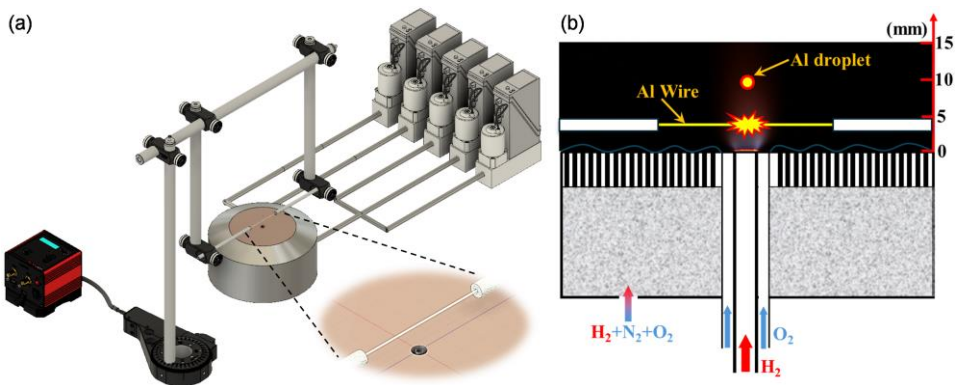


**Figure 3.1:** Experimental setup. (a) overall setup, (b) burner design.

surroundings. The premixed flame can be changed from fuel-rich to lean conditions by varying the gas supply. Thus, the gas composition in post-flame regions can be altered from  $\text{H}_2\text{O}/\text{N}_2$  to  $\text{H}_2\text{O}/\text{N}_2/\text{O}_2$ .

The novelty of this design is that an appropriate high-temperature region in the burner center can be generated to facilitate the formation of one single aluminum droplet. Once the wire moves to the burner center, it gets molten, breaks up, and generates one single burning aluminum droplet that moves upward following the ambient flow. The method demonstrates a reliable way for single aluminum droplet generation that is quite different from previous studies using either wire chopping [42] or direct particle seeding [82]. The single droplet generation process is highly reproducible in experimental practice. The initial size of the produced droplets varies by less than 5% across more than 30 trials.

Table 3.1 summarizes the  $\text{H}_2$  flame conditions used in this work, labeled from F1 to F6. For the central diffusion flame, the  $\text{O}_2$  supply is kept as half of the  $\text{H}_2$  supply for complete consumption of the central  $\text{H}_2$ . In the premixed flat flame, six cases (F1~F6) with varying  $\text{H}_2\text{O}$ ,  $\text{O}_2$ , and  $\text{N}_2$  concentrations in the post-flame gases are considered. The proportions of  $\text{H}_2\text{O}$ ,  $\text{O}_2$ , and  $\text{N}_2$  of the premixed flat flame are estimated assuming the complete consumption of  $\text{H}_2$  while  $\text{N}_2$  only acts as the dilution gas. For the first three cases (F1-F3), the equivalence ratio of the flat flame is set to 1.0, and therefore only  $\text{H}_2\text{O}$  and  $\text{N}_2$  exist in the post-flame gases. Assuming complete consumption of  $\text{H}_2$ , the proportion of  $\text{H}_2\text{O}$  varies from 30.6% to 18.4% by mole fraction from case F1 to F3. For cases F4-F6, the fraction of  $\text{O}_2$  varies from 30.7% to 10.7% while the concentration of  $\text{H}_2\text{O}$  is maintained at ~25%. When transitioning the flame conditions from F1–F3 to F4–F6, the oxidizers for aluminum combustion change from an  $\text{H}_2\text{O}/\text{N}_2$  mixture to an  $\text{H}_2\text{O}/\text{O}_2/\text{N}_2$  mixture. A key advantage of this setup is its ability to sustain a hot steam environment, facilitating the investigation of the  $\text{Al}-\text{H}_2\text{O}$  reaction. Notably, very few experimental studies to date have offered a detailed characterization of  $\text{Al}-\text{H}_2\text{O}$  combustion [60].

**Table 3.1:** Operating conditions of the burner: the central diffusion flame and surrounding premixed flame.

Flame cases	Central diffusion flame reactants (SLM) <sup>a</sup>		Surrounding premixed flat flame						
	$\text{H}_2$	$\text{O}_2$	Reactants (SLM)				Products (vol%) <sup>c</sup>		
			$\text{H}_2$	$\text{O}_2$	$\text{N}_2$	$\Phi$ <sup>b</sup>	$\text{O}_2$	$\text{H}_2\text{O}$	$\text{N}_2$
F1	0.50	0.25	6.30	3.15	14.30	1	0	30.6	69.4
F2	0.50	0.25	5.20	2.60	15.95	1	0	24.6	75.4
F3	0.50	0.25	4.00	2.00	17.75	1	0	18.4	81.6
F4	0.40	0.20	5.33	9.13	9.29	0.29	30.7	25.3	44.0
F5	0.40	0.20	5.26	7.00	11.49	0.38	20.7	24.9	54.4
F6	0.40	0.20	5.30	4.90	13.55	0.54	10.7	25.1	64.2

<sup>a</sup>Standard liter per minute.

<sup>b</sup>Equivalence ratio

<sup>c</sup>Products of the premixed flat flame assuming complete consumption of  $\text{H}_2$

Additionally, the total mass flow rate of the gas supply remains constant at  $23.75 \text{ L} \cdot \text{min}^{-1}$  through all tests, to achieve a comparable velocity field for different cases. Note that the burnt gases from both the diffusion and premixed flames build the oxidizing environment for aluminum combustion. However, in the low central region ( $r < 5 \text{ mm}$ ,  $h < 15 \text{ mm}$ ), the diffusion flame dominates the oxidizing environment for aluminum droplets, while the premixed flat flame rather provides a hot co-flow. The setup for single droplet combustion is employed in **Papers I-V**.

### 3.1.2 Burning aluminum droplets

Aluminum wires with diameters of  $250 \text{ }\mu\text{m}$ ,  $125 \text{ }\mu\text{m}$ , and  $65 \text{ }\mu\text{m}$  are used. The length of the aluminum wires used for each trial is around  $3 \text{ cm}$ . The purity of the wires (Goodfellow GmbH) is around  $99.5\%$ . Figure 3.2 shows a typical long-exposure photo that integrates the entire combustion process, including droplet generation, steady combustion, and unsteady combustion. Once the aluminum wire moves to the burner center, an individual aluminum droplet is generated from the molten wire. The droplet moves upward following the flow field. It goes through a steady

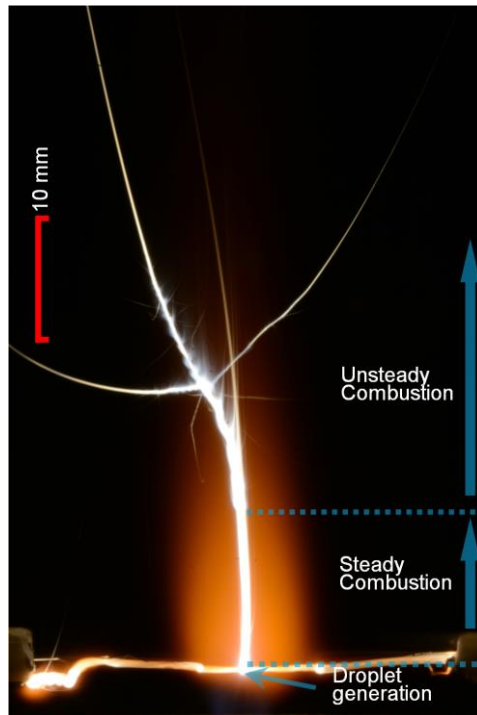


**Figure 3.2:** A typical long-exposure ( $1.6 \text{ s}$ ) image capturing the entire combustion process of an aluminum wire in case F4, including aluminum droplet generation, steady combustion, and unsteady combustion.

combustion characterized by a smooth trajectory, followed by an unsteady combustion stage with spiral-structure trajectory and droplet fragmentation. The combustion process happens at a micrometer scale in milliseconds.

Representative sequences of ignition and combustion of aluminum wire ( $D = 250\ \mu\text{m}$ ) in flame case F1 and F4 are shown in Figure 3.3(a) and Figure 3.3(b), respectively. The images are taken by a high-speed color camera with high magnification ( $8.7\ \mu\text{m}/\text{pixel}$ ).

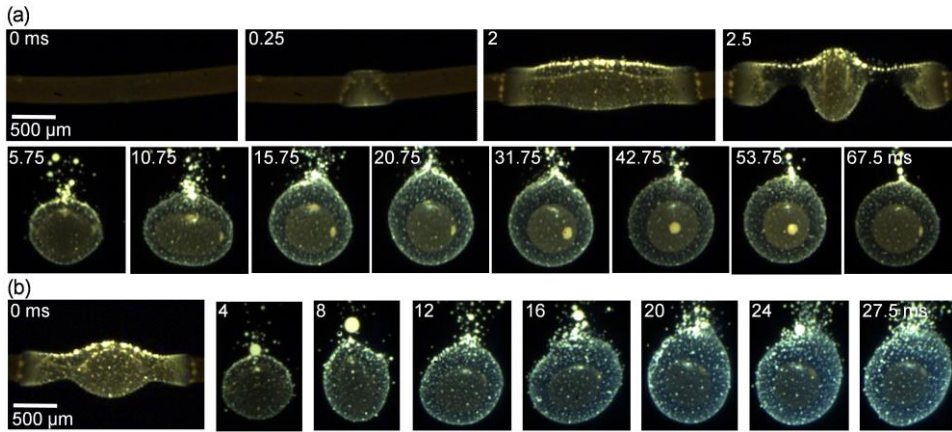


**Figure 3.3:** Sequential images of the aluminum combustion process, including the droplet generation and steady combustion processes. The sequence is taken from a color high-speed camera at 4 000 fps. (a) aluminum wire  $D = 250\ \mu\text{m}$  burning in flame F1, (b) aluminum wire  $D = 250\ \mu\text{m}$  burning in flame F4.

The process in Figure 3.3(a) can be described in the following stages:

- 1) Wire ignition and droplet generation: The wire reaches the center position at 0 ms and gets ignited as the alumina coating collapses at 0.25 ms. By 2 ms, a liquid aluminum cylinder roughly 1.6 mm in length is formed and encapsulated by a vapor-phase flame layer. Due to the upward laminar flow, the visible flame front is lifted further from the top of the molten aluminum cylinder than from the bottom. Aluminum sub-oxides generated by homogeneous gas-phase reactions subsequently condense into alumina clusters or nanoparticles. These alumina products then agglomerate into micrometer particles downstream, which are more prominent on the top side of the flame front due to convective flow. At 2.5 ms, the wire breaks up under surface tension, forming a burning aluminum droplet approximately 500  $\mu\text{m}$  in diameter. Similar ignition phenomena are observed for wires tested in both flame F1 and flame F4.
- 2) Flame development: From 5.75 ms to 20.75 ms, the flame front envelops the aluminum droplet as the standoff distance between the droplet surface



and the outer flame front continuously increases until it stabilizes. The flame front is characterized by a thin bright layer composed of high-temperature condensed alumina droplets. The aluminum droplet vibrates due to the drag force resulting from the wire breakup. The flame shape closely follows the morphological changes of the droplet during the vibration, indicating the prompt formation of the flame front at a new position whenever the aluminum surface shifts.

- 3) Symmetric combustion: Between 31.75 ms and 67.5 ms, symmetric steady vapor-phase combustion is observed until the particle moves out of view. During this period, a thin flame front fully envelops the central aluminum droplet, representing the symmetric phase of aluminum combustion. Additionally, a small oxide cap attached to the aluminum droplet surface is observed, believed to originate from the melting and shrinking of the alumina coating layer due to surface tension during the wire ignition process.

Figure 3.3(b) illustrates the ignition and combustion of the wires in flame F4, where an aluminum droplet of similar size forms under a symmetric combustion phase. Compared to the process in flame F1, significantly more oxide particles are generated that are visibly distributed throughout the flame front in flame F4, indicating that aluminum burns more rapidly in the oxygenated environment. Additionally, the emission intensity of the case in flame F4 is approximately six times higher than that observed in flame F1. These differences highlight the enhanced combustion of aluminum in an oxygen-contained atmosphere.

Figure 3.4(a) and (b) display sequential images illustrating the ignition of thinner ( $D = 125\ \mu\text{m}$ ) aluminum wires in flames F1 and F4, respectively. An oxide cap is identified as the bright part of a burning droplet due to its relatively higher emissivity compared to aluminum. For the thinner wires, two different burning states are observed depending on the initial size of the oxide cap on the aluminum surface. In addition to the symmetric combustion phase, an asymmetric phase shows

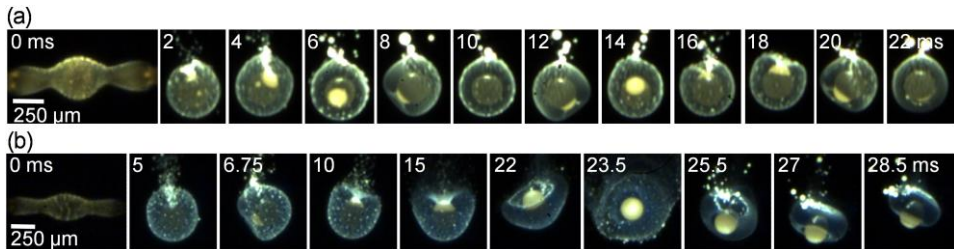


**Figure 3.4:** Sequential images of aluminum combustion process from droplet generation to asymmetric combustion stage. The sequence is taken from a color high-speed camera. (a) aluminum wire  $D = 125\ \mu\text{m}$  burning in flame F1, (b) aluminum wire  $D = 125\ \mu\text{m}$  burning in flame F4.

up, during which the flame sheet can only envelop part of the aluminum droplet. If the initial oxide cap is relatively small, the burning aluminum droplets will go through a symmetric phase in the observation period, like the behavior of the droplet presented in Figure 3.3. However, if the covered area of the initial oxide exceeds a certain limit, the burning aluminum particle will quickly transform into an asymmetric combustion phase as shown in Figure 3.4. The larger oxide cap occupies a bigger portion of the aluminum surface and partly blocks the evaporation of aluminum, which distorts the flame front. The oxide cap keeps growing due to the continual oxide deposition and the particle keeps spinning.

### 3.1.3 Burning Al-Mg alloy

The combustion of Al-Mg alloy is experimentally studied using wires with a diameter of 200  $\mu\text{m}$ . The wires have a composition of 96.5% Al, 3.1% Mg, 0.1% Fe, 0.2% Si, and 0.1 % others. The sequence of a typical combustion process is shown in Figure 3.5.

The wire ignition and combustion process are depicted in Figure 3.5(a). Compared to pure aluminum wires in Figure 3.3 and Figure 3.4, major differences have been observed in the ignition behavior during 0–15 ms, when localized ignition events happen at certain points due to surface oxidation. The localized ignition phenomena are initialized by gradual shedding of the alumina coating, highlighted by the blue dashed circle at 3 ms. The failure of the protective coating exposes the metal core to oxidizers, and then local oxidation occurs indicated by the bright spots (red dashed circles at 3.25 ms). Similar local ignition behaviors repeat and heat the wire until its complete ignition at around 16 ms. Unlike the ignition of the pure aluminum wires which lead to reproducible droplet generation, the entirely different behaviors of the alloy wires cannot generate single burning droplets in a stable manner. During 16–25 ms, vapor-phase combustion happens along the wire. This stage is characterized by the breakup of the molten coating, the outward effluence of liquid metals, and the formation of ball-shaped burning tips. A faint flame is instantly formed around the tip, and clouds of bright micrometer particles are then observable at the top due to the upward co-flow. The wire is consumed by the detached diffusion-flame around the metal balls, which regresses rapidly back to the ceramic tube holders. The energy released during the combustion continuously provides latent heat for the evaporation of the metal, and a gas-phase combustion is self-sustained.

Due to wire break-up or micro explosion, a single burning droplet can be occasionally produced after wire ignition, as shown in Figure 3.5(b). After preheating, a short portion of the wire, indicated in the red dashed circle at 2 ms, breaks up and ignites. It shrinks into a spherical droplet ( $D \approx 250 \mu\text{m}$ ) and the vapor-phase combustion starts. Similar droplet combustion phenomena are

observed as the ones in Figure 3.3 and Figure 3.4. More descriptions of the combustion of Al-Mg alloy wires are presented in **Paper V**.

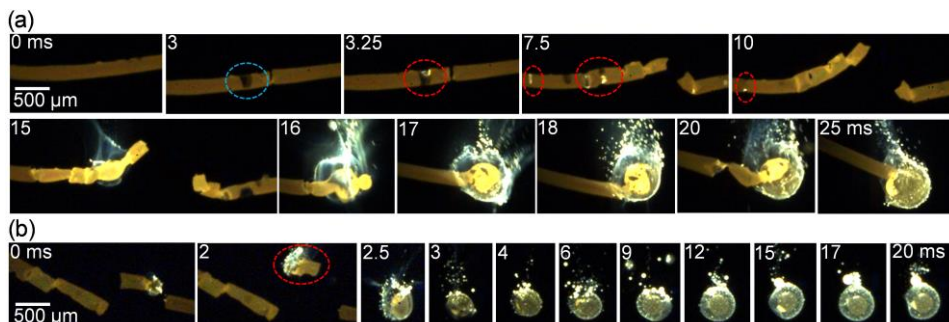


**Figure 3.5:** Sequential images of Al-Mg wire ( $D = 200 \mu\text{m}$ ) burning in flame F1. (a) wire ignition and wire combustion. (b) droplet generation and droplet combustion.

## 3.2 Aluminum dust flame

Figure 3.6(a) shows a schematic of the flat flame burner and the particle feeding system. A modified flat flame burner fueled with premixed Ar/CH<sub>4</sub>/O<sub>2</sub> mixture (mass flow rates of 16.8, 6.0, and 20.0 L.min<sup>-1</sup>, respectively) is employed to produce a laminar flat flame, thus generating a high-temperature and controllable oxidizing environment for the ignition and combustion of aluminum particles. The composition of the burnt gases downstream of the flat flame is calculated to be O<sub>2</sub> (18.7%), CO<sub>2</sub> (14.0%), H<sub>2</sub>O (28.0%), and Ar (39.3%) assuming that CH<sub>4</sub> goes to complete oxidization with O<sub>2</sub> and produces CO<sub>2</sub> and H<sub>2</sub>O only. The temperature of the exhaust gas along the centerline of the burner at different heights (height above the burner, HAB) is measured using a B-type thermocouple (OMEGA, P30R-008,  $D = 200 \mu\text{m}$ ). The uncertainty of the readout temperature from the thermocouple is about  $\pm 5 \text{ K}$ . As shown in Figure 3.6(b), the temperature along the centerline increases from around 1750 K at 3 mm HAB to around 2000 K at around 9 mm HAB and maintains around 1950–2000 K between 9–21 mm HAB.

The aluminum particles used (GoodFellow Cambridge Limited, AL00-PD-000131) are generated by air atomization and have a purity of  $> 99.9\%$ . The particles have irregular shapes as shown in the Scanning Electron Microscope (SEM) images in Figure 3.6(c). The frequency histogram of the area-equivalent particle diameter is determined by a calibrated optical microscope (Olympus). It is shown that the majority (over 75%) of the particles have diameters less than  $5 \mu\text{m}$ . The powder is placed onto the positive electrode of a capacitor and aerosolized between the electrodes by activating a high voltage of around 13 kV. An air flow transports the

aerosolized particles through the central tube (inner diameter 1 mm) towards the burner where the aerosol exits at a nominal velocity of 0.25 m/s.

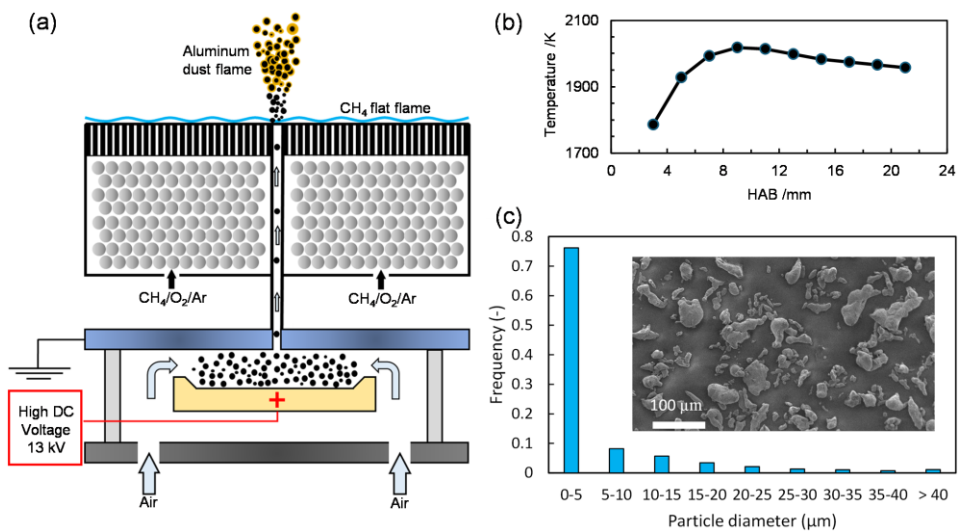


**Figure 3.6:** Dust flame burner design. (a) powder supply with burner schematic, (b) temperature along the burner centerline, (c) SEM images of aluminum powders and their size distribution.

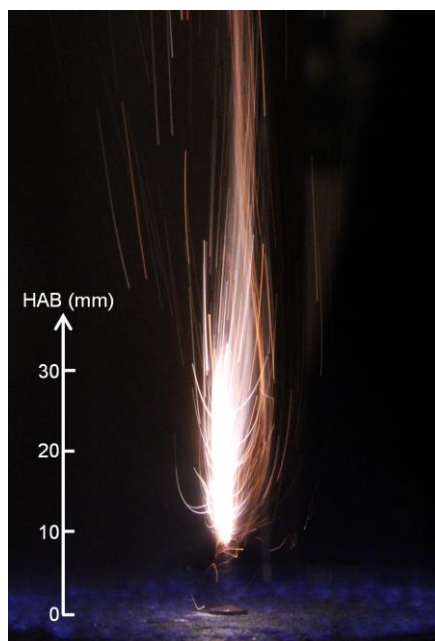


**Figure 3.7:** A photograph of the lifted aluminum dust flame acquired with a digital camera (exposure time: 1/800 s).

Figure 3.7 depicts a photograph of the lifted aluminum particle cloud flame acquired with a digital camera. The incandescence of the burning particles thus appears as bright traces in the image. The fresh particles are ignited at around 7 mm HAB as visualized by the strong and sudden increase in light intensity. The flame extends to about 25 mm HAB. Unlike the setup in Figure 3.1 where a hot diffusion flame is introduced as an igniter with a temperature above 2600 K, the key feature of the dust flame is that the temperature of the ignition source, i.e. the pilot methane flame, does not reach the alumina melting point (2327 K). By increasing the powder supply density thus strengthening the particle-particle interaction, a lifted aluminum dust flame can be ignited and stabilized. The setup of aluminum dust flame is employed in **Paper VI** and **Paper VII**.

## 4. Optical diagnostic methods

Various optical diagnostic techniques are developed to catch the transient aluminum combustion process at a micrometer scale, including (1) high-speed incandescence-shadowgraph imaging, (2) high-speed RGB pyrometry imaging, (3) spatially-resolved laser absorption spectroscopy, (4) darkfield and brightfield microscopy.

### 4.1 High-speed incandescence-shadowgraph imaging

A novel optical diagnostic setup is designed to simultaneously image the flame incandescence and shadowgraphs of burning aluminum droplets. The incandescence images capture the morphological evolution of the wire melting, the formation of the aluminum droplet, and the aluminum droplet combustion. The shadowgraph images are used to show the generation and the distribution of alumina smoke, and the droplet size changes. The simultaneous detections enable quantitative determination of key burning parameters, such as flame standoff ratio, flame thickness, and droplet evaporation rate, with high spatiotemporal resolution.

A typical optical layout is schematically shown in Figure 4.1. A continuous wave (CW) laser at wavelength 405 nm and average power 8 W is used for backlight illumination. The 405 nm wavelength is chosen to efficiently suppress the incandescence emission from the hot droplets. The laser beam is expanded and re-collimated by a telescope made of spherical lenses. Two diffusers provide homogeneous illumination of the field of view (FOV). A 50/50 beam splitter separates the signals behind a Nikon objective (focal length 135 mm, f#11). Two high-speed cameras (Phantom VEO 710L) are operated at 10 000 fps with a sensor of  $600 \times 1280$  pixels. A long extension tube is inserted between the Nikon objective and the cameras to allow for magnified imaging, which yielded a FOV of  $\sim 5.2 \times 11.1 \text{ mm}^2$  and a projected pixel size of  $\sim 8.7 \text{ }\mu\text{m}/\text{pixel}$ . The transmitted light is filtered with an interference filter ( $405 \pm 5 \text{ nm}$ , Edmund Optics, #65-678), thus imaging the shadowgraphs of the particles onto the first high-speed camera. The reflected light is filtered with a long-pass filter ( $> 450 \text{ nm}$ , Edmund Optics, #64-698), thus imaging incandescence onto the sensor of the second high-speed camera. The cameras are synchronized and simultaneously triggered with the wire positioning device. The exposure time for the camera imaging shadowgraphs is  $5 \text{ }\mu\text{s}$ , while the exposure time for the camera imaging incandescence is adjusted between

3  $\mu\text{s}$  and 9  $\mu\text{s}$ , for imaging optimization. The cameras are arranged in a way that they visualize the same FOV.

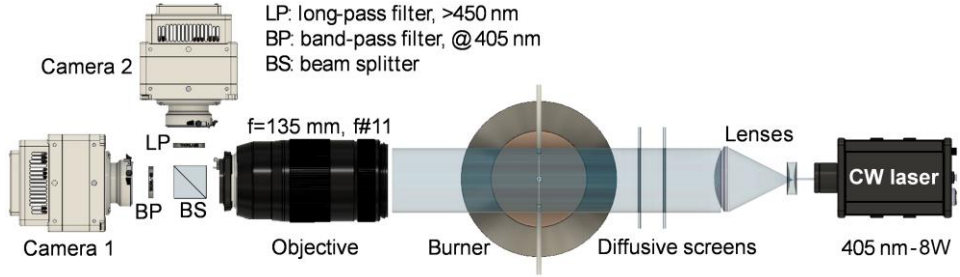


**Figure 4.1:** Setup for incandescence-shadowgraph imaging.

Figure 4.2 shows a typical burning aluminum droplet in the symmetric phase. The bottom image shows the incandescence signal and the top image shows the corresponding shadowgraph of all the condensed phases within the FOV. The alumina smoke of nano-to-micrometer droplets downstream can be captured in the shadowgraph images whereas the incandescence images show mostly larger micrometer alumina droplets. The simultaneous recordings complementarily reveal the multi-phase combustion behaviors. The incandescence-shadowgraph technique is employed in **Paper I** and **Paper III**.

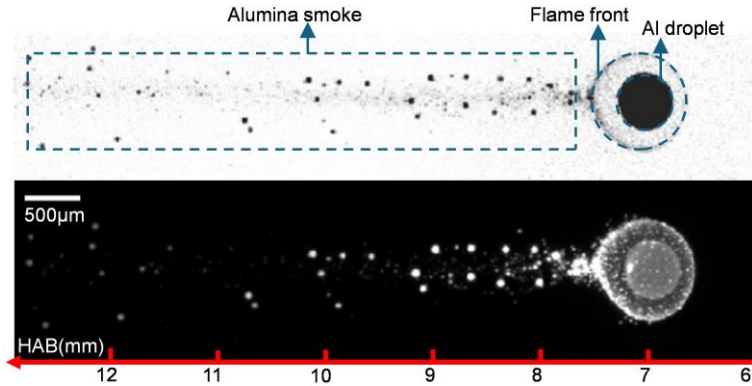


**Figure 4.2:** Simultaneous imaging of a burning Al droplet. The bottom image shows the incandescence and the corresponding shadowgraph is shown at the top.

## 4.2 High-speed RGB pyrometry imaging

### 4.2.1 Theoretical background

Multi-spectral pyrometry is a common method for surface temperature measurements [83]. It measures the radiation intensities in several wavelength ranges, and the ratios of these signals are used to derive the temperature. In this work, a high-speed color camera (Photron AX100) with three color channels, i.e. red (R), green (G), and blue (B), is used to determine the surface temperature in the transient combustion process. Thus, the method is named RGB pyrometry.

RGB pyrometry requires a good characterization of the spectral responses for the whole imaging system. Figure 4.3 presents a normalized spectral response for the three channels provided by the manufacturer. The curves display the spectral response of the sensor in the wavelength range from around 350 nm to 700 nm. However, we found in our measurements that there might be an infrared light leakage on the blue channel. Meanwhile, the signals detected by the red channel are generally much higher than the other two channels. Thus, proper optical filters are needed to block the IR transmission and to balance the signal level over the three channels. The study uses a 2 mm thick  $50 \times 50 \text{ mm}^2$  Schott filter BG38. The chosen glass filter has a transmission curve as shown in Figure 4.3, and can effectively suppress the red signals while maintaining the sensitivity of green and blue channels.

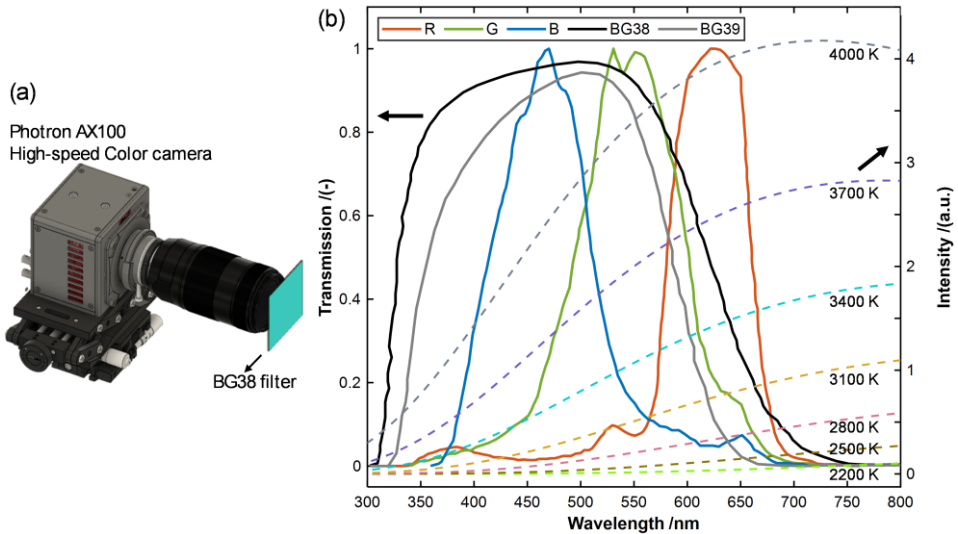


**Figure 4.3:** Solid curves: normalized response curves of the R/G/B channels of the RGB camera and the transmission curve of the BG38 and BG39 filters. Dashed curves: calculated blackbody radiation distribution at different temperatures covering from 2200 K to 4000 K.



It is worth noting that the sensor response might be different from the specification of the manufacturer for individual cameras.

The dashed lines shown in Figure 4.3 present the black-body radiation for temperatures from 2200 K to 4000 K. According to Wien's displacement law, the peak wavelengths for the curves are generally longer than 720 nm, which is outside of the sensor transmission cut-off wavelength ( $\approx 700$  nm). Consequently, within the wavelength and temperature range of interest, a monotonic relationship between the intensity ratio (between the R/G/B channels) and temperature is guaranteed in the RGB pyrometry.

The theoretical foundation of RGB pyrometry is Planck's Law introduced in Section 2.5.1. For a surface of temperature  $T$ , the thermal radiative emission power  $I(\lambda, T)$  per unit area and solid angle is determined by Eq. (2.2). Therefore, the detected signal over one camera channel,  $E_c$ , can be expressed as an integral of  $I(\lambda, T)$  over the response curve of the channels,

$$E_c = \tau \int_{\lambda_1}^{\lambda_2} \eta(\lambda) I(\lambda, T) d\lambda \quad (4.1)$$

where  $\tau$  indicates the integral time,  $\eta(\lambda)$  accounts for the spectral response of the imaging system.  $\lambda_1$  and  $\lambda_2$  are the low and high limits of the filter bandwidth, which are approximately 400 and 700 nm. Thus, the temperature-ratio look-up table  $R_T$  can be derived through Eq. (4.2).

$$R_T = \frac{E_{c1}}{E_{c2}} = \frac{\int_{\lambda_1}^{\lambda_2} \eta_{c1}(\lambda) \varepsilon(\lambda) \lambda^{(-5)} \times (e^{\frac{hc}{\lambda kT}} - 1)^{-1} d\lambda}{\int_{\lambda_1}^{\lambda_2} \eta_{c2}(\lambda) \varepsilon(\lambda) \lambda^{(-5)} \times (e^{\frac{hc}{\lambda kT}} - 1)^{-1} d\lambda} \quad (4.2)$$

Here,  $\eta_{c1}(\lambda)$  and  $\eta_{c2}(\lambda)$  denote the effective response function over wavelength for each color channel. It is worth noting that during the calibration procedure, both signals on the green and red channels are generally more than five times higher than the blue one over the approachable temperature range. Owing to the relatively low signal-to-noise ratio of the blue channel, only the green/red (G/R) ratio is employed for direct temperature measurement in the current study.

#### 4.2.2 Calibration

According to Eq. (4.2), a ratio-temperature ( $R$ - $T$ ) relationship is determined based on the spectral responses shown in Figure 4.3 and the graybody assumption. The calculation is shown as the dashed line denoted as 'Initial calibration' in Figure 4.4. Due to the uncertainty of the spectral responses of the sensor, more direct calibrations on calibration targets with known temperatures are conducted to get an optimized  $R$ - $T$  lookup table. As illustrated in Figure 4.4, three different targets

covering different temperature ranges have been used: (1) B-type thermocouple (OMEGA, P30R-008), 1626–1953 K, (2) SiC fibers, 1788–2028 K, (3) liquid alumina at its melting point (2327 K). The calibrations lead to an ‘optimized calibration’ curve in Figure 4.4, which is used for temperature determination.

An uncertainty analysis has shown that the detection noise of the camera sensor results in a  $\pm 60$  K error. This value reflects the uncertainty of the relative temperature difference obtained in the work. Moreover, due to the lack of calibration in the temperature range higher than 2400 K, a systematic uncertainty would be introduced from the extrapolation. As shown in Figure 4.4, the optimized calibration curve is located in between the linear fitting and the initial calibration curve. At a temperature of 3200 K derived from the current calibration, the temperature difference between the three curves is about  $\pm 300$  K at the same ratio. Therefore, we estimated that the system error of the absolute temperature value at 3200 K is within  $\pm 300$  K and the systematic error would increase when the temperature increases and decreases when the temperature drops. The RGB pyrometry technique is employed in **Paper II**.

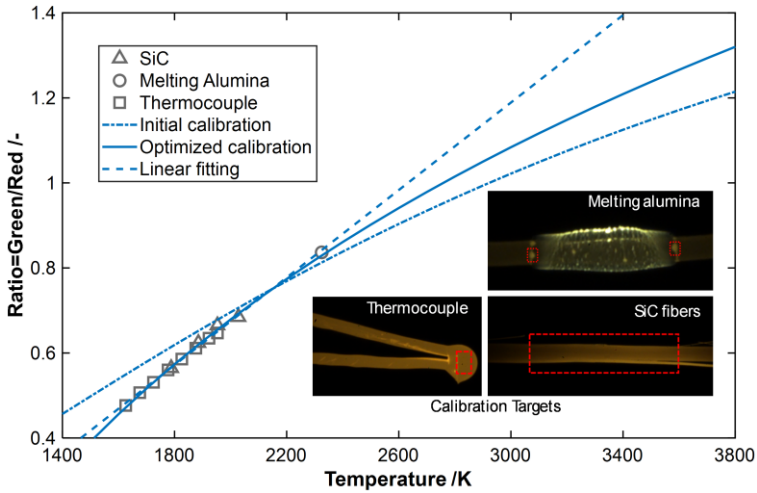


**Figure 4.4:** Calibration curves of the RGB pyrometry with the images of the calibration targets. The BG38 filter is used.

### 4.2.3 Optimized RGB pyrometry

The RGB pyrometry is further optimized in two aspects: 1) the blue channel is included for temperature determination; 2) calibrations in the high-temperature range ( $>3000$  K) are conducted.

In the previous section, the G/R ratio is used to determine temperature. However, at high temperatures, the G/R ratio becomes less sensitive to temperature changes,

because of the narrow separation in wavelength of the transmissions over the two channels. Consequently, even significant temperature fluctuations result in only small variations in the G/R ratio, resulting in an increased measurement uncertainty. In contrast, the blue/red (B/R) ratio has higher sensitivity to temperature, as the wavelength separation between these two channels is wider. To use this ratio, the relative signal level on the blue channel compared to the red channel should be enhanced to improve the signal-to-noise ratio. Therefore, a BG39 filter is used, the transmission of which is presented in Figure 4.3. Compared to BG38, BG39 suppresses the red and green transmission while largely maintaining the blue signal.

Calibrations in the high-temperature range are performed using a tungsten filament (Thorlabs SLS301B) as the calibration target. Previous studies [84,85] have shown that tungsten is not a perfect graybody, i.e., has an emissivity varying with wavelength. Specifically, from 400 to 700 nm, the emissivity decreases linearly by approximately 10% from 0.46 to 0.42 at 2800 K. This emissivity variation is accounted for in the calibration procedures. By adjusting the power source, the tungsten filament temperature is varied from around 2600 K to 3200 K. The filament temperature is determined by fitting its spectra to Planck's law. In addition, calibrations in the lower temperature range are conducted using a thermocouple and melting alumina. The final calibration curves, illustrating  $R$ - $T$  relationships, are presented in Figure 4.5. Due to its high sensitivity to temperature, the B/R relationship is used for temperature determination. The measurement uncertainty of the optimized RGB pyrometry originating from the sensor noise is around  $\pm 60$  K. It should be noted that the alumina droplets in the current work are simply treated as graybody for simplification. However, as stated in Section 2.5.1, the emissivity

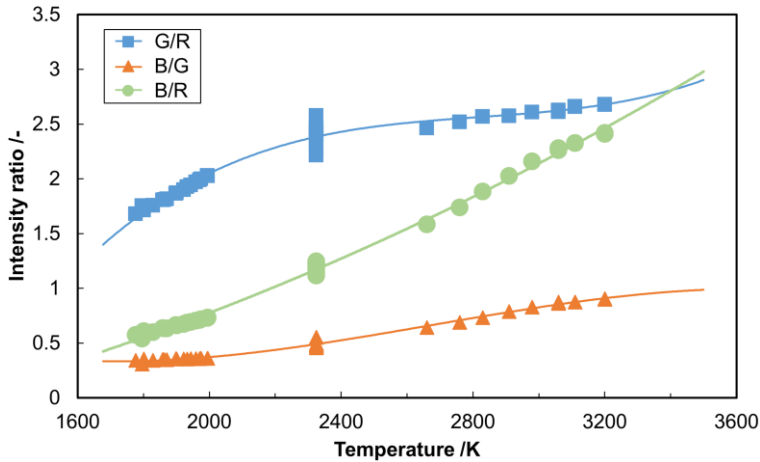


**Figure 4.5:** Calibration curves for the optimized RGB pyrometry. The BG39 filter is used.

of nano-to-micrometer alumina droplets remains largely unknown, and they may not behave as perfect graybody. This uncertainty will also introduce systematic errors in the temperature measurements.

## 4.3 Spatially-resolved laser absorption spectroscopy of Al atom

### 4.3.1 Experimental setup

Spatially-resolved laser absorption spectroscopy (SLAS) and a shadowgraph imaging system are implemented simultaneously to detect the distribution of Al atoms around a burning aluminum droplet. SLAS utilizes a single-mode tunable diode laser (TOPTICA, DL Pro100) with a laser linewidth below 1.0 MHz as the illumination source. The diode laser wavelength is tuned from 396.000 to 396.300 nm, encompassing the peak absorption line of the Al atom at 396.152 nm corresponding to the  $^2P_{3/2} \rightarrow ^2S_{1/2}$  transition. The laser beam is expanded and recollimated using a set of mirrors and lenses before entering the flame region. The transmitted laser light is then captured by high-speed camera#1 (Photron FASTCAM SA5). In this configuration, the camera detects light extinction resulting from both the absorption by Al atoms and the scattering and absorption of condensed-phase materials, including the aluminum droplet core and alumina products.

The shadowgraph system utilizes a continuous wave (CW) laser at 532 nm. The laser beam is aligned with the path of the diode laser and is directed to high-speed camera #2 (Photron FASTCAM AX200). At this wavelength, light extinction occurs solely due to the absorption and scattering by the aluminum droplet core and alumina products. Consequently, the shadowgraph images provide detailed information on the location and size of the aluminum core and the alumina condensation layer. This capability is particularly important when the edges of the aluminum droplet cannot be discerned in images from camera #1, due to strong resonant absorption near wavelength 396.152 nm.

The beam from the diode laser first passes through a beam sampler (M #1, Thorlabs DMSP425), directing 1% of the light to a wavelength meter (HighFinesse WS5) for wavelength measurement with an absolute accuracy of 3.0 GHz. To guide the 396 nm and the 532 nm laser beam into the same optical path, a short-pass dichroic mirror (M #4, Thorlabs DMSP425, 425 nm cutoff) is used to transmit 396 nm laser light while reflecting 532 nm laser light. Subsequently, both laser beams are guided by two high-reflection mirrors (M #5 and M #6), then expanded and collimated using a combination of concave and convex lenses. It produces cylindrical laser beams that illuminate the entire FOV. After passing through the burning aluminum

droplet, the transmitted signals are focused by an objective lens (Nikon, 135 mm, f/16). Another short-pass dichroic mirror (M#7) is used to ensure simultaneous recordings of the two high-speed cameras. Camera #1 is equipped with Bandpass Filter #1 centered at 394 nm (full-width at half maximum [FWHM]: 10 nm, Edmund Optics, #65-192), and camera #2 is equipped with Bandpass Filter #2 centered at 532 nm (FWHM: 3.7 nm, Edmund Optics, #68-970). Both cameras are triggered by the wire feeding device and synchronized to operate at a framing rate of 6 400 Hz. The FOV is optimized to approximately  $5.7 \times 5.7 \text{ mm}^2$  with a sensor of  $1024 \times 1024$  pixels, resulting in around  $5.6 \text{ }\mu\text{m}/\text{pixel}$ . The exposure times are set to approximately  $10 \text{ }\mu\text{s}$  for camera #1 and  $3.3 \text{ }\mu\text{s}$  for camera #2.

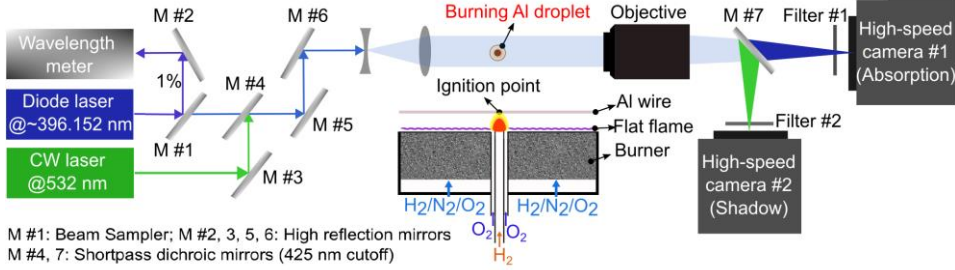


**Figure 4.6:** Experimental setup for simultaneous spatially-resolved laser absorption spectroscopy and shadowgraph imaging.

#### 4.3.2 Number density determination from SLAS measurements

The number density of Al atoms around a burning aluminum droplet is determined following the Beer-Lambert law [86,87]:

$$\frac{I_e(\nu)}{I_0(\nu)} = e^{-\alpha(\nu)} \quad (4.3)$$

where  $\nu$  is the light frequency,  $I_0(\nu)$  and  $I_e(\nu)$  are the incident and transmitted laser light intensity, respectively.  $\alpha(\nu)$  denotes the frequency-dependent absorbance, which is proportional to the absorption cross-section  $\sigma(\nu)$ , optical path length  $L$ , and the number density  $N$  of Al atoms at the  $^2\text{P}_{3/2}$  state:

$$\alpha(\nu) = \sigma(\nu)LN \quad (4.4)$$

$\sigma(\nu)$  is expressed as:

$$\sigma(\nu) = \frac{h\nu_0 B_{12} \chi(\nu, N, T)}{c} \quad (4.5)$$

where  $h$  is Planck's constant,  $\nu_0$  is the central frequency of the absorption,  $B_{12}$  represents the Einstein absorption coefficient,  $\chi(\nu, N, T)$  indicates the area-

normalized line shape function,  $T$  is the temperature, and  $c$  is the speed of light. The Einstein coefficient  $B_{12}$  can be calculated as:

$$B_{12} = \left(\frac{g_2}{g_1}\right) \left(\frac{c^3}{8\pi h \nu^3}\right) A_{21} \quad (4.6)$$

where  $g_2$  and  $g_1$  represent the degeneracy of states 2 and 1 of the transition, respectively and  $A_{21}$  is the Einstein spontaneous emission coefficient. The constants are presented in Table 2.2. By substituting Eq. (4.5) into Eq. (4.4), rearranging and then integrating Eq. (4.4), we can determine the number density  $N$  as follows:

$$N = \frac{c}{h\nu_0 B_{12} L} \int_{\nu} \alpha(\nu) d\nu \quad (4.7)$$

According to Eq. (4.7), the determination of  $\int_{\nu} \alpha(\nu) d\nu$  is the key step to obtain the number density  $N$ .

In the SLAS measurements, both the incident light intensity  $I_0(\nu)$  and the transmitted light intensity  $I_e(\nu)$  are recorded. Thus, the absorbance  $\alpha(\nu)$  can be determined according to Eq. (4.3). By scanning the laser frequency around the central resonant frequency, the absorbance  $\alpha(\nu)$  is obtained at various frequencies. The measured absorbance  $\alpha^m(\nu)$  is then fitted using a Voigt profile [88] which accounts for both the Doppler and collision broadening effects. From the fitted absorbance  $\alpha^f(\nu)$ , the number density  $N$  is calculated based on Eq. (4.7). It is important to note that the experiments only measure the number density of Al atoms in the  $^2P_{3/2}$  ground state, excluding those in the  $^2P_{1/2}$  state. The number density of atoms in the  $^2P_{1/2}$  state is subsequently determined using Eq. (2.4). Adding up those two groups presents the total atom population in the ground state. The combined absorption-shadowgraph technique is used in **Paper IV**.

## 4.4 Darkfield and brightfield microscopy

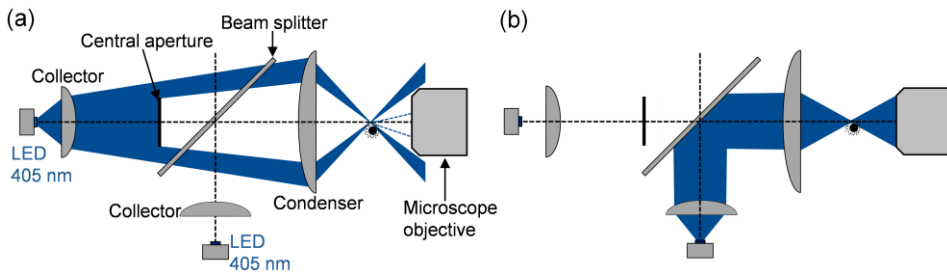
### 4.4.1 Optical layout

Figure 4.7 shows the optical layout of (a) darkfield and (b) brightfield microscopy, employed to image light scattering and extinction, respectively. Light from two LEDs (Roschwege UV-LED, 405 nm, FWHM: 10 nm) is used to illuminate the FOV on the centerline of the aluminum dust flame. The two LEDs are alternately pulsed by a diode driver (Picolas, LDP-V 50-100 V3.3) to image either transmission or scattered light. The pulse durations are 2.2 and 0.5  $\mu$ s for darkfield and brightfield microscopy, respectively.

In the darkfield microscopy, the light from the LED is collected by an aspheric lens ( $f = 16$  mm,  $d = 25$  mm) and imaged onto the spherical condenser lens ( $f = 75$  mm,  $d = 50$  mm) with a magnification of approximately 25. An aperture with a diameter of 20 mm blocks the central part of the beam between the collector and the condenser. The light passes a beam splitter (Edmund Optics, 51.76 mm<sup>2</sup>, 70% transmission and 30% reflection at 405 nm) and the condenser focuses the light and illuminates an area of around  $2.5 \times 2.5$  mm<sup>2</sup> in the FOV. Blocking the central part of the beam ensures that only light with a numerical aperture greater than that of the microscope objective (0.15) illuminates the FOV. Consequently, light is only collected and imaged when objects, i.e., particles and droplets, in the FOV refract, reflect, or scatter the incident light, otherwise, the image remains dark.

In brightfield microscopy, the light is collected and directed toward the condenser lens. The LED is imaged with a magnification of 12.5 onto the condenser, ensuring that the numerical aperture of the illumination matches that of the collecting microscope objective. Consequently, the brightfield image displays transmitted light that has been attenuated by condensed-phase materials, effectively enabling shadowgraphy.

On the detection side, a microscope (Infinity K2 DistaMax, CF-4 front lens) images the transmitted or scattered light onto the camera (Photron SA-Z) sensor. This yielded a projected pixel size of  $2.5$   $\mu\text{m}/\text{pixel}$ . The focal depth of the imaging system is found to be around  $130$   $\mu\text{m}$ . The exposure time is set to  $2$   $\mu\text{s}$  in all measurements. To suppress natural incandescence from hot aluminum and alumina, a bandpass filter centered at 405 nm (Edmund Optics, #65–678, FWHM: 10 nm) is inserted into the microscope. The camera is operated either in full resolution ( $1024 \times 1024$  pixels) at 20 000 fps or with a cropped sensor ( $160 \times 384$  pixels) at 200 kfps. The latter with an interval of  $5$   $\mu\text{s}$  between two frames is employed for quasi-simultaneous imaging of light extinction and scattering.



**Figure 4.7:** Top view of the optical layout of (a) darkfield microscopy and (b) brightfield microscopy.

#### 4.4.2 Volume and size determination for droplets in the Rayleigh regime

Similar to Eq. (4.3), light extinction  $\tau_e$  is defined based on the Beer-Lambert law:

$$\tau_e = -\log \left( \frac{I_e}{I_0} \right) \quad (4.8)$$

The transmission after light extinction,  $I_e$ , is expressed as:

$$I_e = I_0 - (S_{s,\text{total}} + S_a) \quad (4.9)$$

where  $S_{s,\text{total}}$  and  $S_a$  are the light intensities that are lost due to scattering and absorption, respectively. We define the transmission after scattering only,  $I_s = I_0 - S_{s,\text{total}}$ , and the transmission after absorption only,  $I_a = I_0 - S_a$ . Assuming that absorption and scattering are independent, and both cause exponential attenuation, we decompose the Eq. (4.8) into two separate terms:

$$\tau_a = -\log \left( \frac{I_a}{I_0} \right) \quad (4.10)$$

$$\tau_s = -\log \left( \frac{I_s}{I_0} \right) \quad (4.11)$$

Thus, light extinction  $\tau_e$  in the probing volume is the sum of light absorption  $\tau_a$ , and scattering,  $\tau_s$ , i.e.  $\tau_e = \tau_a + \tau_s$ .

The volume fraction  $f_v$  of particles in a suspension can be related to light extinction as follows [89]:

$$f_v = \frac{\lambda \cdot \tau_e}{K_e \cdot L} \quad (4.12)$$

Here,  $K_e$  is the dimensionless extinction coefficient,  $L$  is the path length through the extinction medium, and  $\lambda$  is the wavelength of the light. In principle, when knowing  $K_e$ , the volume fraction can be calculated from the measured transmission. However,  $K_e$  is a complex function of the particle shape, particle diameter  $D_p$ , and complex refractive index  $m$ . Meanwhile,  $K_e$  is the sum of the respective dimensionless absorption and scattering coefficients  $K_e = K_a + K_s$ . Inserting this into Eq. (4.12) and rearranging it, the relation becomes:

$$\tau_e = \frac{K_a \cdot f_v \cdot L}{\lambda} + \frac{K_s \cdot f_v \cdot L}{\lambda} \quad (4.13)$$

Separate two components in Eq. (4.13) and designate them as absorption ( $\tau_a$ ), and scattering ( $\tau_s$ ), respectively. By considering only the absorption component, we obtain the following relation:

$$f_v = \frac{\lambda \cdot \tau_a}{K_a \cdot L} \quad (4.14)$$



For spherical particles in the Rayleigh regime, i.e.,  $\frac{\pi \cdot D_p}{\lambda} < 1$ ,  $K_e$ ,  $K_s$ , and  $K_a$  can be expressed analytically. While  $K_e$  and  $K_s$  are functions of the particle size even in the Rayleigh regime,  $K_a$  becomes a size-independent function of the absorption function  $E(m)$  of the material [90]:

$$K_a = 6 \cdot \pi \cdot E(m) \quad (4.15)$$

The absorption function,  $E(m)$ , is obtained from the complex refractive index,  $m$ , of aluminum. The refractive index for aluminum at around 3500 K is taken as  $1.84+0.01i$  and consequently, the absorption function is 0.0038 [89]. As the exact absorption path length is not known at every pixel, the total volume, i.e., integrated along the line-of-sight, of the nanoparticles at that pixel can be quantified instead by multiplying Eq. (4.14) with  $L$  and the square of the projected pixel size,  $L_{\text{pixel}}$ :

$$V = \frac{\lambda \cdot \tau_a}{6 \cdot \pi \cdot E(m)} \cdot L_{\text{pixel}}^2 \quad (4.16)$$

In this work, the quantification is made on the nanoparticles that lie in the Rayleigh regime. At 405 nm, the maximum particle size in this regime, i.e.,  $\frac{\pi \cdot D_p}{\lambda} = 1$ , becomes 130 nm. The following quantifications on the nano alumina droplets only consider the size range below 130 nm.

Figure 4.8 shows the absorption and scattering cross sections and the single-scattering albedo of alumina at 3500 K as a function of droplet size. The cross sections are calculated from Mie theory [73] implemented from ref. [91]. The single-scattering albedo is the ratio of scattering and extinction  $\frac{\tau_s}{\tau_s + \tau_a}$ , which is equal to the ratio of the corresponding cross sections,  $\frac{c_s}{c_s + c_a}$ . As in the Rayleigh regime, the absorption cross-section scales with  $D_p^3$  while the scattering cross-section scales with  $D_p^6$ , the former is larger for small particles. The albedo increases from near 0 at 1 nm to 0.95 at 130 nm. Thus, the particle size linking to the albedo in the Rayleigh regime can be used to determine the particle size.

In the experiments, the bright-field microscopy captures the extinction from both scattering and absorption, while the dark-field microscopy detects the scattering only. Combining the two measurements with proper postprocessing, light absorption, and scattering can be decomposed experimentally. Consequently, the determination of the absorption  $\tau_a$  allows the quantification of nanoparticle volume based on Eq. (4.16), meanwhile, the nanoparticle size can be determined by measuring the single scattering albedo. Darkfield and brightfield microscopy are utilized in **Paper VII**.

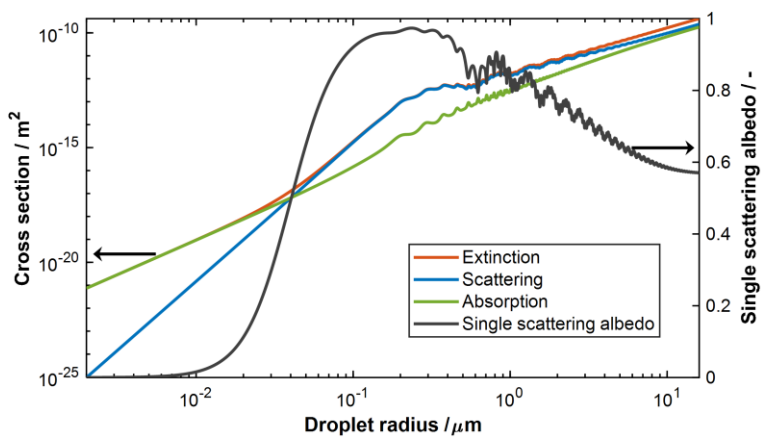


**Figure 4.8:** Absorption and scattering cross sections and the single-scattering albedo of alumina at 3500 K.

## 5. Aluminum combustion characterization

The transient micro-structures of aluminum flames are characterized by different well-designed optical diagnostic techniques. Section 5.1-5.4 presents the results on single aluminum droplets. Section 5.5 shows results from measurements of the aluminum dust flame.

### 5.1 Flame structure of single burning aluminum droplets

#### 5.1.1 From wire ignition to symmetric combustion

Figure 5.1 shows a representative sequence of ignition and combustion of the 250  $\mu\text{m}$  aluminum wire in the steam case F1, captured with the incandescence-shadowgraph imaging. The processes can be described in the following three stages: (I) aluminum ignition and droplet generation; (II) droplet evaporation and flame development; and (III) steady combustion. Detailed descriptions of these processes are provided in Section 3.1.2. The top row of each stage shows the incandescence images, and the corresponding shadowgraph images are shown beneath.

Compared to Figure 3.3, Figure 5.1 offers additional insights into the distribution of alumina products through simultaneous shadowgraph recordings. During the third stage (19.6 ms to 47.6 ms), the droplet maintains a quasi-steady, diffusion-limited combustion mode. Numerous alumina droplets continuously emerge on the thin, bright flame sheet and subsequently detach from the flame at the top. Due to the low Stokes number, the alumina droplets (nano-to-micrometer) tend to follow the surrounding gas flow, making them effective tracers for the flow field around the burning droplet. Throughout the steady combustion stage, the flame standoff distance remains nearly constant, indicating that the alumina layer encapsulating the aluminum droplet forms a stagnation plane with zero radial velocities. Newly generated alumina droplets on the flame sheet slip upward along the stagnation plane, agglomerate into larger particles, are transported downstream by the gas flow, and detach from the flame sheet at the downstream tip. Moreover, the thickness of the flame sheet is analyzed using Abel inversion of the projected profile of the flame

incandescence and optical depth in the shadowgraph, revealing a flame thickness of about  $50\ \mu\text{m}$  for the burning droplet in Figure 5.1. The flame standoff ratio is around 1.75 and it slightly increases with decreasing droplet size. Details of the flame thickness determination and flame standoff ratio are introduced in **Paper I**.

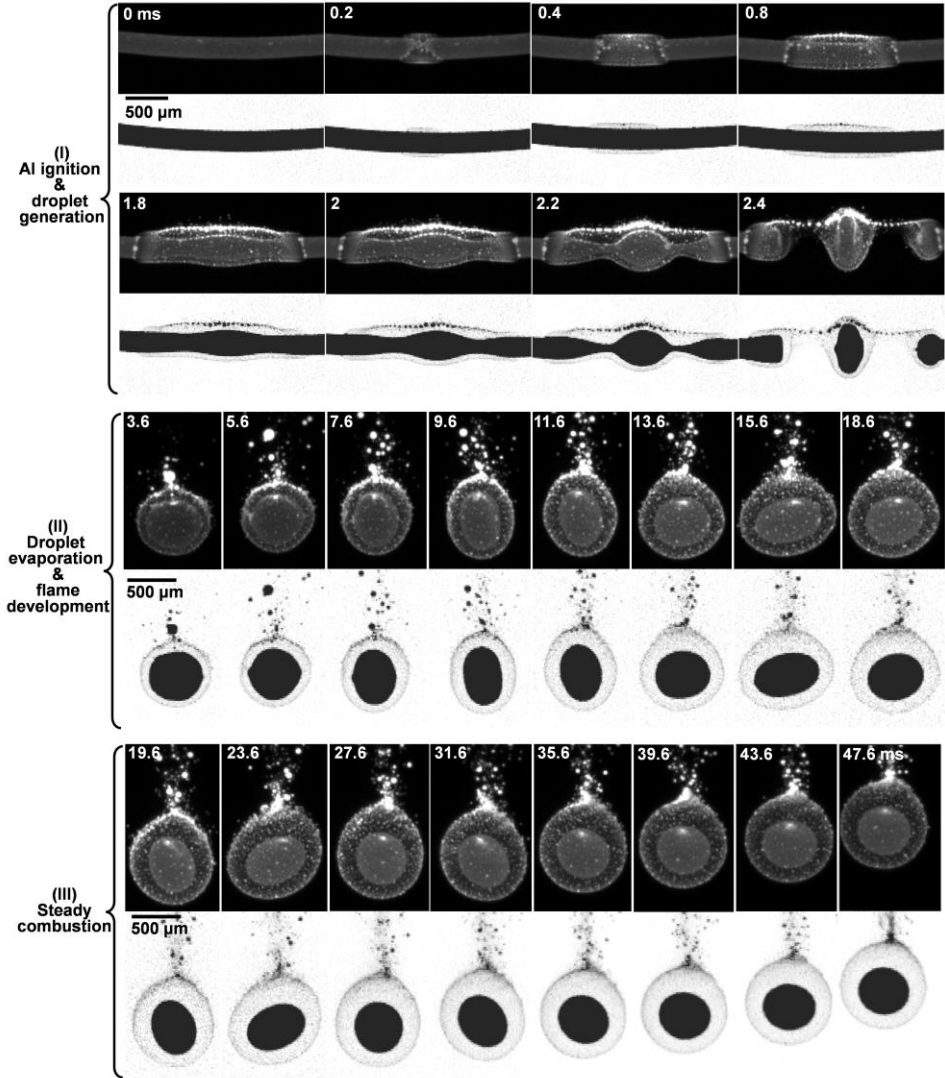


**Figure 5.1:** Ignition and combustion sequences of the  $250\ \mu\text{m}$  aluminum wire in steam case F1 from the simultaneous recording of incandescence and shadowgraph. The whole process can be divided into three stages: (I) aluminum ignition and droplet generation, (II) droplet evaporation and flame development, and (III) steady combustion. The top row of each stage shows the incandescence emission, and the image beneath shows the corresponding shadowgraph.

Based on the shadowgraph images, the evaporation rate,  $\beta_v = \frac{dD_d^2}{dt}$ , of the Al droplets is determined from the shrinking rate of the droplet projected area. Table 5.1 summarizes the evaporation rates of aluminum droplets with different initial sizes in flame cases F1 and F4. More than five samples are averaged in each case. First, the evaporation rate is highest in case F4. The oxygen addition to the steam environment approximately doubled the evaporation rate. Second, a size dependence on the evaporation rate is also found, where  $\beta_v$  decreases as the droplet size decreases. The size dependence is attributed to the difference in the convective effects with varying droplet sizes. Higher slip velocities for larger droplets enhance the mass transfer by displacing the species near the flame front, thus creating a steeper concentration gradient and enhancing the evaporation rate. At the same time, the higher slip velocities cause an enhanced heat transfer between the surrounding gas flow and the flame sheet. It may also enhance the evaporation of the larger droplets.

**Table 5.1.** Experimental evaporation rates ( $\beta_v$ ) of aluminum droplets.

Flame cases	$\beta_v$ [mm <sup>2</sup> /s]		
	$D_d \sim 550 \mu\text{m}$	$D_d \sim 240 \mu\text{m}$	$D_d \sim 110 \mu\text{m}$
F1	$1.0 \pm 0.2$	$0.6 \pm 0.1$	$0.35 \pm 0.1$
F4	-	$1.2 \pm 0.2$	$0.8 \pm 0.1$

### 5.1.2 Unsteady combustion

The unsteady combustion behaviors of an aluminum droplet with an initial diameter of 110  $\mu\text{m}$  are shown in Figure 5.2. From 0-10 ms, a burning aluminum droplet is generated and goes through a symmetric combustion stage, like the larger one shown in Figure 5.1. During this period, alumina products condense into droplets and are trapped in the thin layer of the flame sheet, gradually agglomerating into a large alumina satellite droplet orbiting the aluminum core. This satellite, approximately 110  $\mu\text{m}$  in size, reaches a temperature of about 3420 K.

At 10.4 ms, the alumina satellite starts to collide with the central aluminum core. Then, the two immiscible parts coalesce into one binary Janus droplet, with an alumina cap on one side and aluminum on the other. As the alumina cap is more than 600 K hotter than the liquid Al, the temperature difference between the two parts triggers the ejection of aluminum vapor between 11–11.6 ms. The heat transfer from the hot alumina cap to the contacted aluminum produces large amounts of aluminum vapor, leading to a ‘cone-shaped’ ejection from the interface between the liquid aluminum and the oxide cap. The ejected Al vapor is mixed with the surrounding oxidizer and gets quickly oxidized and condenses into numerous nano-

to-micrometer alumina droplets, shown as a plume of smoke in the shadowgraph images. The rapid evaporation leads to a dramatic size shrinking of the aluminum core.

By 11.7 ms, the alumina cap nearly encapsulates the remaining aluminum core, and the ejection pauses. Still, thermal equilibrium has not yet been reached within the droplet. The vapor pressure of the aluminum core continuously increases with the increased temperature until a rapid expansion of the oxide shell, resulting in droplet fragmentation at 11.8 ms shown as a micro explosion of the droplet. At 12.3 ms, the largest fragment, containing both alumina and aluminum, shows a cap structure like that at 11 ms, allowing the asymmetric combustion to continue. The comprehensive

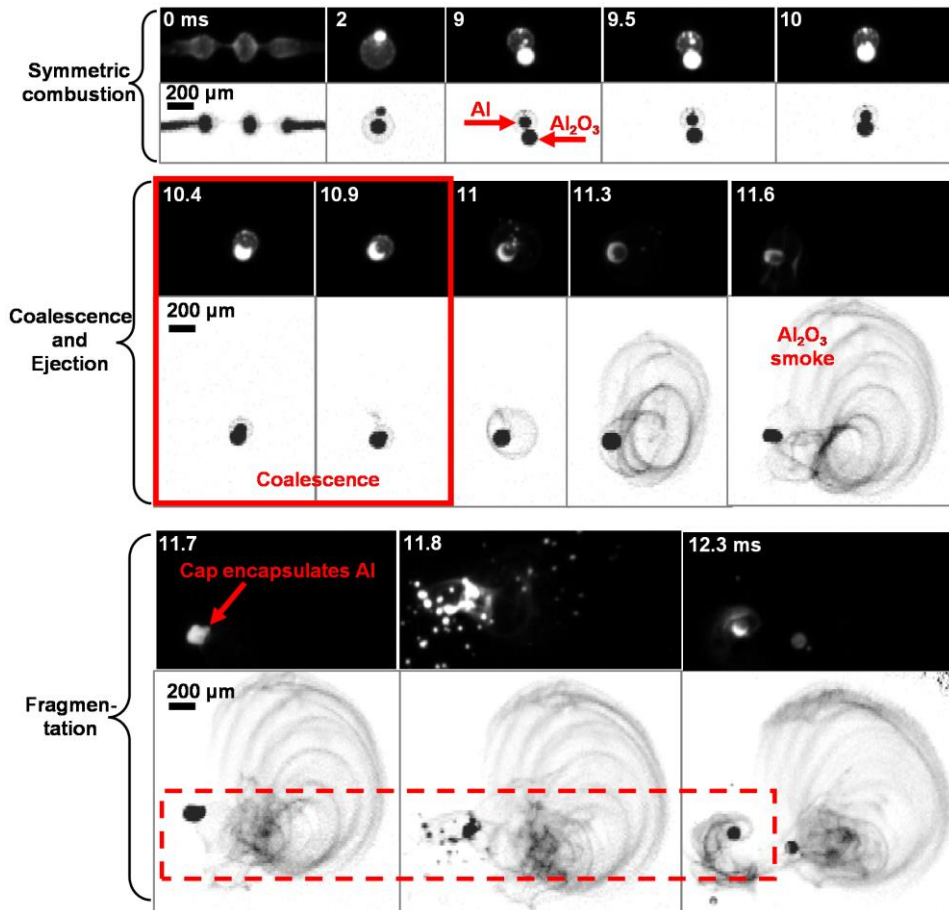


**Figure 5.2:** Sequential image pair of simultaneously recorded incandescence and shadowgraph of burning aluminum droplets ( $D_{Al} \approx 110 \mu\text{m}$ ), showing ignition, symmetric combustion, eruption, and fragmentation in the oxygenated case F4.

characterization of the Janus droplet structure, temperature evolution, and nano oxide formation during the unsteady combustion is described in **Paper III**.

### 5.1.3 Theoretical analysis during symmetric combustion

A conceptual model is proposed to describe the symmetric combustion of an aluminum droplet, as illustrated in Figure 5.3. The proposed model incorporates a laminar flow field around the burning aluminum droplet and the distribution of alumina products. Aluminum atoms vaporized from the droplet surface form a strong Stefan flow. This evaporation is sustained by the heat feedback from the flame sheet via thermal conduction and radiation. The aluminum vapor is oxidized when it mixes with the surrounding oxidizer, forming a thin diffusion flame. A flame sheet represented by a thin layer of hot nano-to-micrometer alumina droplets is located at a relatively stable distance from the aluminum droplet surface, indicating a stagnated flow pattern around the droplet. With zero radial speed in the flame region, the alumina droplets move along the flame sheet downstream and accumulate at the trailing edge of the wake. The conceptual model enables quantitative analysis of heat release, heat transfer, and droplet evaporation.

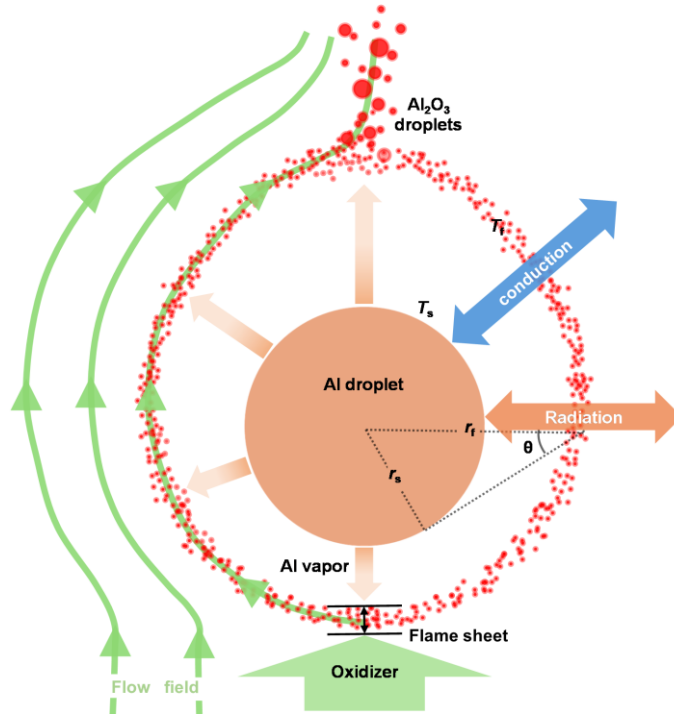


**Figure 5.3:** Conceptual model of the flame structure around a burning aluminum droplet in a laminar flow.

The heat of reaction for aluminum/steam oxidation under 1 atm and 2600 K is given by  $\text{Al(g)} + 1.5\text{H}_2\text{O(g)} = 0.5\text{Al}_2\text{O}_3\text{(l)} + 1.5\text{H}_2\text{(g)}$ ,  $\Delta H = -690$  kJ/mol. The enthalpies of the chemical species are taken from ref. [92]. The mass flow rate,  $\dot{m}$ , of the aluminum vapor from the droplet surface is calculated as:

$$\dot{m} = \frac{dm}{dt} = \frac{\pi}{4} \rho_l D_d \beta_v \quad (5.1)$$

where the density of liquid aluminum at 2650 K,  $\rho_l$ , is taken from ref. [93].  $D_d$  denotes the droplet diameter and  $t$  is the burning time. The total heat release is estimated from the one-step reaction assuming a complete consumption of the vaporized aluminum,  $\Phi_{\text{reaction}} = \frac{\Delta H}{(27 \times 10^{-3} \text{ kg/mol})} \dot{m} = 20.8$  W. The latent heat for droplet evaporation in Figure 5.1 is estimated to  $\Phi_{\text{eva}} = \Delta h_v \times \dot{m} = 8.87$  W, where  $\Delta h_v = 10.9$  MJ/kg [93]. The latent heat is provided by the flame sheet. For this droplet, a rough estimation suggests that around  $\frac{\Phi_{\text{eva}}}{\Phi_{\text{reaction}}} \approx 40\%$  of heat released from aluminum combustion is provided for aluminum evaporation in the steady combustion stage.

The flame sheet sustains aluminum evaporation through thermal conduction and radiation, i.e.  $\Phi_{\text{eva}} = \Phi_{\text{con,s}} + \Phi_{\text{rad}}$ , where  $\Phi_{\text{con,s}}$  denotes the conductive heat flow at the droplet surface and  $\Phi_{\text{rad}}$  denotes the radiation heat flow. As the surface temperatures are constant throughout the investigated period of evaporation, the heat and mass transfer occur in a steady state. To determine the contribution of thermal conduction and convection (Stefan flow) in evaporating the droplet, the one-dimensional temperature profile between the flame sheet and the droplet surface is required. Based on the combustion model sketched in Figure 5.3, the steady-state one-dimensional energy conservation equation in the gas phase between the droplet surface and the flame sheet is formulated as [94]:

$$r^2 \rho c_p v \frac{dT}{dr} = \frac{d}{dr} \left( k r^2 \frac{dT}{dr} \right) \quad (5.2)$$

where the left-hand side represents the change in the internal energy of a fluid element due to convective effects, i.e., the Stefan flow, and the right hand side represents thermal conduction. Note that the radiative effects only involve the boundary condition, and the gas between the flame and the droplet does not absorb or emit heat. Several assumptions are made in the following analysis, including (a) constant physical and chemical properties along the radius, e.g., thermal conductivity  $k$  and heat capacity  $c_p$ , (b) chemical reactions releasing heat occurring at the flame position  $r = r_f$ , (c) spherical symmetry, (d) quasi-steady state, and (e) Lewis number,  $Le = 1$ . We consider the following cases:

- 1) First, when neglecting the Stefan flow ( $v_{\text{st}} = 0$ ), it becomes a pure conduction process (the left side of Eq. (5.2) becomes zero) between the droplet surface ( $r = r_s = 275$   $\mu\text{m}$ ) and the flame ( $r = r_f = 480$   $\mu\text{m}$ ) with



corresponding temperatures,  $T_s$  and  $T_f$ . Then, Eq. (5.2) can be simplified as  $\frac{d}{dr} \left( kr^2 \frac{dT}{dr} \right) = 0$  with  $r_s \leq r \leq r_f$ . Integrating the equation with respect to  $r$  and applying the boundary condition  $T_s = 2650$  K,  $T_f = 3400$  K, we can derive the temperature profile and its gradient, as shown in Figure 5.4. The thermal conductivity of aluminum vapor is taken as  $0.1$  W/(K·m) at around  $3000$  K. Thus, calculating the conductive heat flow to the droplet surface yields  $\Phi_{\text{con},s} = Ak \left( \frac{dT}{dr} \right)_s = 0.61$  W.

- 2) Then, if we take the Stefan flow into consideration, integrating Eq. (5.2) to  $r$  and applying the temperature boundary conditions as well as the constant mass flow rate condition,  $\dot{m} = 4\pi r^2 \rho v = 4\pi r_s^2 \rho_s v_s$ , the temperature profile and its gradient are derived and shown in Figure 5.4. The conductive heat flow at the droplet surface, in this case, is  $\Phi_{\text{con},s} = Ak \left( \frac{dT}{dr} \right)_s = 0.40$  W. This indicates that heat conduction is weakened due to the Stefan flow effect.
- 3) Significant uncertainties may come from the assumption of constant thermal conductivity. Near the aluminum surface, the gas is dominated by aluminum vapor. So, the thermal conductivity at the droplet surface,  $k_s$ , is assumed to be around  $0.1$  W/(m·K). While at the flame position  $r_f$ , we assume the reactants, Al(g) and H<sub>2</sub>O(g), are consumed, and the gas mixture consists of 55% H<sub>2</sub> and 45% N<sub>2</sub> by mole. The thermal conductivities of H<sub>2</sub> and N<sub>2</sub> at  $3400$  K are  $1.3$  [72,95] and  $0.1$  W/(K·m) [96], respectively. Therefore, the thermal conductivity of the gas mixture in the flame sheet,  $k_f$ , is estimated to be around  $0.76$  W/(K·m). Assuming a linear distribution of  $k$ , we get the thermal conductivity  $k(r) = -0.7854 + 3219.5r$ . Again, applying the boundary conditions for Eq. (5.2), we get the temperature profile as shown in Figure 5.4. Therefore, at the droplet surface, the conductive heat flow becomes  $\Phi_{\text{con},s} = Ak_s \left( \frac{dT}{dr} \right)_s = 1.43$  W.

In the scenarios discussed above, the thermal conduction,  $\Phi_{\text{con},s}$ , alone is insufficient to compensate for the latent heat of vaporization,  $\Phi_{\text{eva}}$ . Additionally, uncertainties may arise from the assumption that heat release occurs exclusively at the flame sheet. In reality, chemical reactions may also take place between the flame sheet and the droplet surface, significantly altering the temperature profile. Therefore, additional heat source terms should be incorporated into Eq. (5.2), which requires more detailed studies of the chemical kinetics.

For a discussion on radiative heat transfer, we assume a spherical shell with the same radius ( $r_f$ ) and temperature ( $T_f$ ) as the flame sheet, and a droplet with the same radius ( $r_s$ ) and temperature ( $T_s$ ) as the aluminum droplet sitting at the center of the shell, the radiation heat flow from the shell to the droplet surface can be calculated as [72]:

$$\Phi_{\text{rad}} = \frac{\sigma A_s (T_f^4 - T_s^4)}{\frac{1}{\varepsilon_s} + \frac{1 - \varepsilon_f}{\varepsilon_f} \left(\frac{r_s}{r_f}\right)^2} \quad (5.3)$$

where  $\sigma$  denotes the Stefan–Boltzmann constant.  $A_s$  is the droplet surface area.  $\varepsilon_s$  is the emissivity of aluminum at 2650 K, which is taken as 0.2.  $\varepsilon_f$  is the emissivity of alumina at 3400 K, which is taken as 0.8. Finally, the radiation heat from the flame to the droplet,  $\Phi_{\text{rad}}$ , is around 0.9 W. The estimation presented herein assumes the flame sheet to be a solid shell with emissivity equal to that of alumina. However, the flame sheet is an optically thin layer composed of numerous nano-to-micrometer alumina droplets. Consequently, the radiation emitted from this optically thin layer is weaker than that from a solid shell with the same emissivity and temperature. Therefore, the actual radiation heat absorbed by the droplet can be lower than the previously calculated value. Additionally, it is important to note that these calculations provide only preliminary estimates, and the accurate determination of thermal radiation remains largely uncertain due to several factors: (1) The flame sheet contains many fine alumina droplets at high temperatures, whose thermal radiation characteristics are not well understood. (2) The size distribution and number density of alumina droplets within the flame sheet remain unknown. Therefore, understanding the alumina condensation mechanism is crucial for accurately analyzing radiation heat transfer in aluminum combustion.

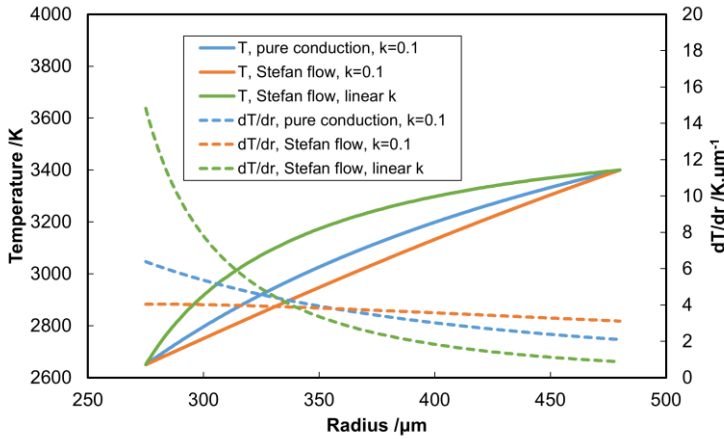


**Figure 5.4:** Radial dependence of temperature and temperature gradient in between droplet surface and flame sheet.

Based on the analysis above, the total heat transfer through conduction and radiation is  $\Phi_{\text{con}} + \Phi_{\text{rad}} \approx 2.33$  W, which accounts for only about 30% of the latent heat of evaporation. Therefore, additional heat sources must significantly contribute to droplet vaporization beyond thermal conduction and radiation from the flame sheet.

One hypothesis is that surface reactions generating gaseous species produce heat on the droplet surface, thereby facilitating the phase change of aluminum. For example, the two principal chain initiation channels, i.e.  $\text{Al} + \text{H}_2\text{O} = \text{AlO} + \text{H}_2$ , and (2)  $\text{Al} + \text{H}_2\text{O} = \text{AlOH} + \text{H}$ , are both exothermic [97]. The water molecule might diffuse through the flame sheet and react with aluminum on the surface, generating heat that enhances the aluminum phase change. Nevertheless, this analysis provides only a brief overview of heat transfer around a burning aluminum droplet. Comprehensive simulation studies that integrate detailed chemical kinetics with alumina condensation are necessary for future optimizations.

## 5.2 Aluminum combustion temperature

### 5.2.1 Temperature evolution during wire ignition and combustion

Figure 5.5 presents the temperature variation during wire ignition and combustion. The average temperature of the ignition part ( $360\ \mu\text{m}$  length) on the wire is measured, as indicated in the wire image at  $118.29\ \text{ms}$  in Figure 5.5. When the aluminum wire is positioned on the burner center, it is heated up from around  $2000\ \text{K}$  to approach the alumina melting point ( $2327\ \text{K}$ ) in about  $118\ \text{ms}$ . Once the protective oxide coating gets melted, the wire temperature dramatically increases to above  $2700\ \text{K}$ . Five typical instants at  $t_1$  to  $t_5$  are shown in Figure 5.5 to illustrate the

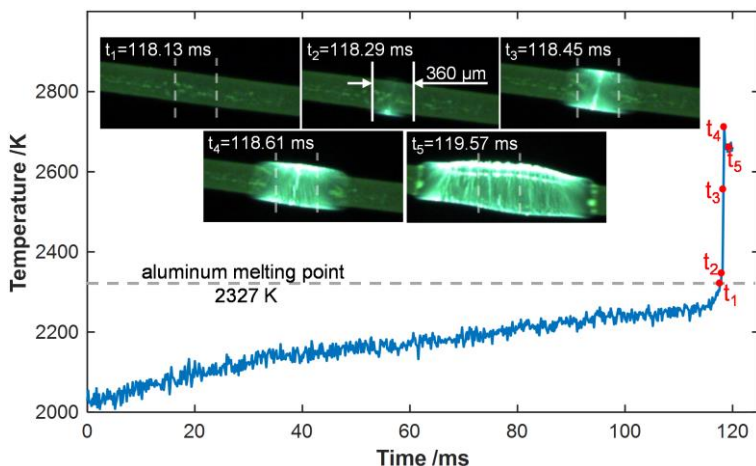


**Figure 5.5:** Temperature evolution during wire ignition and combustion ( $250\ \mu\text{m}$  diameter wire in the steam case F1). The wire morphology from  $t_1$  to  $t_5$  is presented within the diagram. The temperature values are the average temperature of the part with a length of  $360\ \mu\text{m}$  as indicated in the images.

wire morphology evolution. When the aluminum core is exposed to the oxidizer, a flame front characterized by the bright alumina products builds up immediately, encapsulating the aluminum cylinder. The alumina temperature reaches more than 2800 K and it heats the aluminum core to 2327 K. Detailed temperature maps of the wire during ignition and combustion are introduced in **Paper II**.

### 5.2.2 Temperature evolution during droplet development

Aluminum droplets generated from the wire breakup go through a flame development process, during which the position of the flame sheet moves away from near the aluminum droplet surface to a stabilized position. Figure 5.6 presents the changes in the droplet morphology (top row) and the corresponding temperature distribution (bottom row) when burning in the steam case F1. At 0 ms and 7.66 ms, two regions indicated by the blue and red dashed circles, respectively, represent two typical regions on the burning droplet. Within the blue circle area (droplet region), as the flame sheet is optically thin and encapsulates the aluminum droplet, surface radiation from both the aluminum droplet and the flame sheet contributes to the camera signal. Thus, the temperature derived originates from both the aluminum droplet and the flame sheet. Between the blue and red circles, signals are obtained from the flame region consisting of numerous hot nano-to-micrometer alumina droplets. Incandescence in this area comes from flame only, thus the temperature derived represents the flame sheet temperature. Due to the line-of-sight imaging, the incandescence intensity in this region increases from near the droplet surface to the outside flame layer. Thus, the outside flame layer has a higher signal-to-noise ratio, which might lead to lower random errors in temperatures.

As shown in Figure 5.6, the temperatures from both the droplet region and the flame region increase from 0 to 11 ms. The average temperature of these regions and the overall incandescence intensity are presented in Figure 5.7. The overall intensity increases due to increases in temperature and the amount of alumina products. The temperature of the flame rises from around 3000 K to 3380 K, which is mainly due to the increase in the generation rate of alumina droplets. More alumina condenses into a liquid phase in the condensation layer, releasing large amounts of heat. It significantly increases the local temperature of the condensation layer. Meanwhile, the condensation layer with increasing temperature sends back more heat to the aluminum core, resulting in a higher temperature of aluminum and thus higher evaporation rate. The more aluminum evaporates, the more alumina droplets condense and the higher flame temperature. It forms a positive loop in enhancing the combustion rate. At 16.88 ms, the droplet reaches a quasi-steady combustion state, and the flame temperature remains roughly constant. At the same time, the apparent temperature of the droplet region increases from around 2800 K to 3180 K during 0–14 ms, which is generally 200 K lower than the temperature of the flame region.

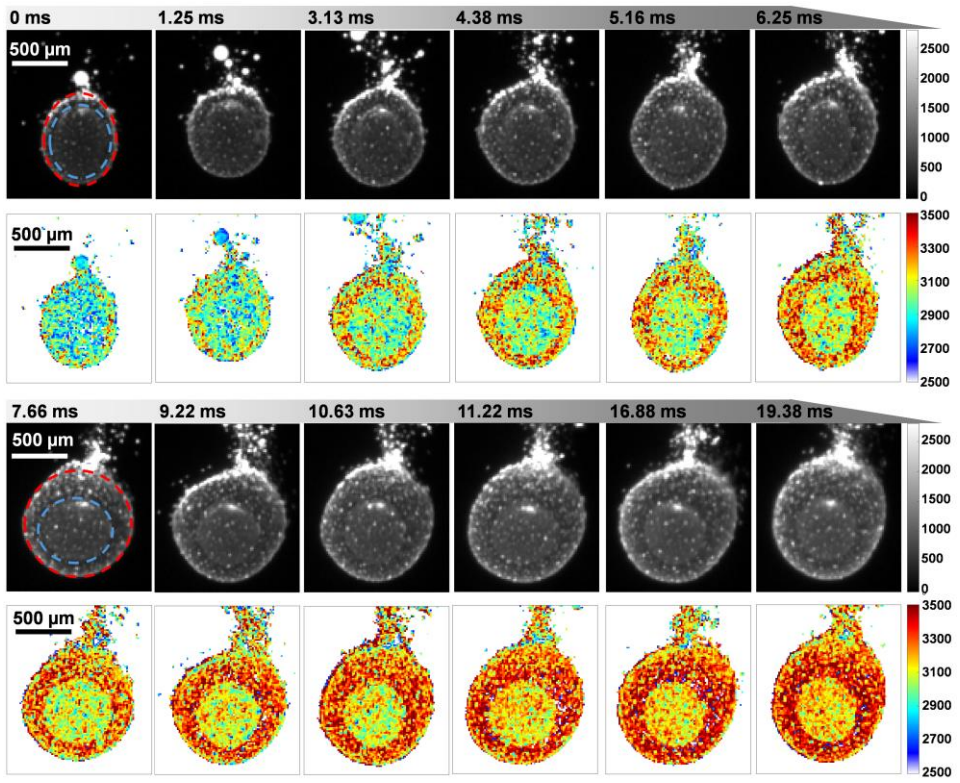


**Figure 5.6:** Droplet burning morphology (top row) and the corresponding temperature distribution (bottom row) during the flame development process in the steam case F1.

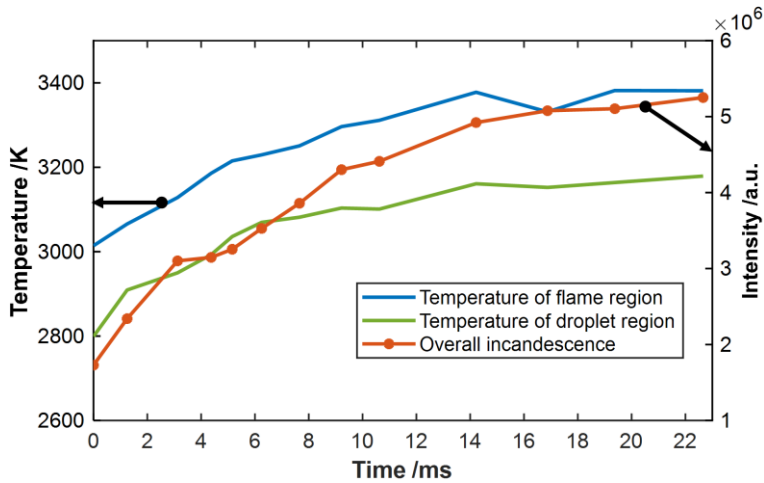


**Figure 5.7:** Temperature evolution of the flame region (blue line) and the droplet region (green line). Evolution of the overall incandescence (orange dotted line).

Although the data do not represent the accurate temperature of the aluminum droplet, the trend reflects its temperature evolution. At 0 ms, the aluminum core formed from wire ignition is close to the alumina melting point (2327 K). As flame develops, its temperature approaches the aluminum boiling point (2790 K).

### 5.2.3 Temperature distribution during symmetric combustion

The temperature and incandescence distribution of the droplets during the steady symmetric combustion are presented in Figure 5.8 and Figure 5.9. The former figure shows the same droplet ( $D_d \approx 550 \mu\text{m}$ ) as the one in Figure 5.6 and the latter figure shows a smaller droplet ( $D_d \approx 240 \mu\text{m}$ ) burning in the same flame condition (steam case F1). Figure 5.8(c) plots the temperature and incandescence distribution along the blue dashed line in Figure 5.8(a). The incandescence is represented by the signal intensity in the R, G, and B channels. The temperature decreases from around 3400 K in the flame region to around 3200 K in the droplet region. In contrast, the small droplet in Figure 5.9 shows a lower combustion temperature. As shown in Figure 5.9(c), the temperature of the flame region is around 3200 K, and the value is around

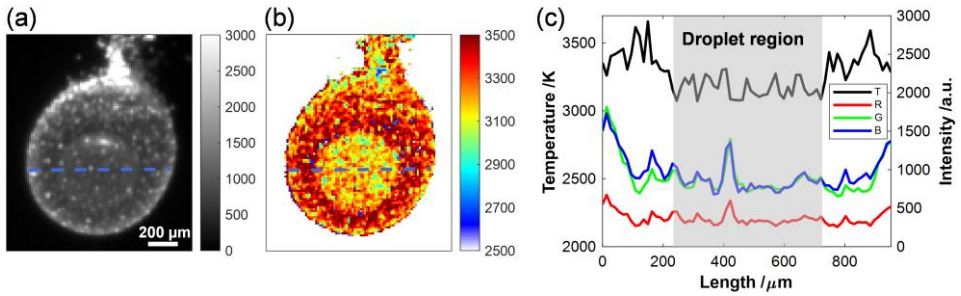


**Figure 5.8:** Temperature and incandescence distribution of the droplet ( $D_d \approx 550 \mu\text{m}$ ) in Figure 5.6 at 22.8 ms. (a) incandescence, (b) temperature map, (c) temperature and emission intensity along the blue dashed line indicated in (a) and (b).

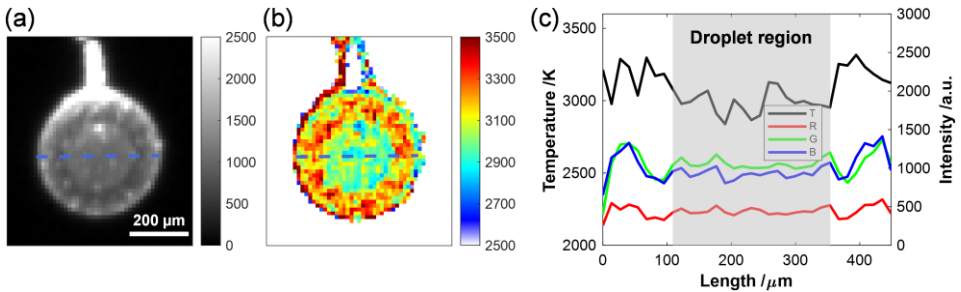


**Figure 5.9:** Temperature and incandescence distribution of the droplet ( $D_d \approx 240 \mu\text{m}$ ) burning in the steams case F1. (a) incandescence, (b) temperature map, (c) temperature and emission intensity along the blue dashed line indicated in (a) and (b).

2900 K in the droplet region. The lower burning temperatures for the smaller droplets might be linked to their smaller evaporation rates as shown in Table 5.1. The higher evaporation rates of larger droplets result in a higher amount of heat release from both chemical reactions and condensation, which might lead to higher flame temperature, i.e. temperature of the alumina products.

### 5.2.4 Temperature distribution during asymmetric combustion

Figure 5.10(a) shows an aluminum droplet burning in the steam case F1 during the asymmetric stage. Part of the aluminum surface is covered with liquid oxide, forming an oxide cap. It stops the aluminum evaporation from the covered region. Thus, there is no flame overlap above the cap, and the temperature on the cap region directly represents its temperature. Figure 5.10(b) presents the temperature map and Figure 5.10(c) shows the temperature and the incandescence distribution along the blue dashed line in Figure 5.10(a). Note that the droplet size is similar to the one in Figure 5.9. and the temperature of the flame regions is roughly the same as well. In the cap region, the incandescence intensity is more than three times higher than the neighboring aluminum part, due to the higher emissivity of liquid alumina. The cap temperature is around 2700 K, which is slightly below the boiling point of aluminum. More information on the cap temperature under different flame conditions is introduced in **Paper II**.

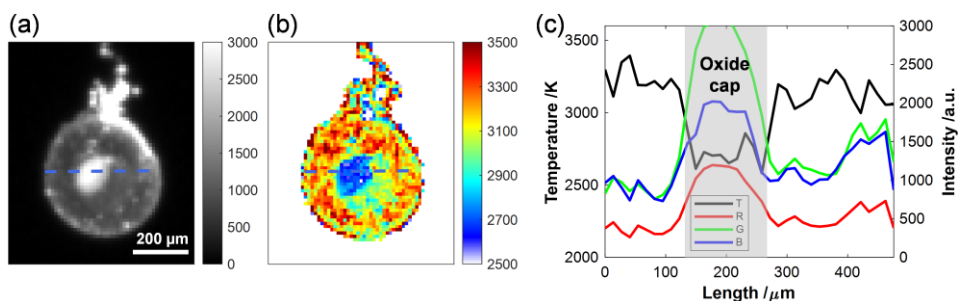


**Figure 5.10:** Temperature and incandescence distribution of the droplet ( $D_0 \sim 240 \mu\text{m}$ ) burning in the steam case F1. The droplet is burning under an asymmetric state where an oxide cap exists on the aluminum droplet. (a) incandescence, (b) temperature map, (c) temperature and emission intensity along the blue dashed line indicated in (a) and (b).

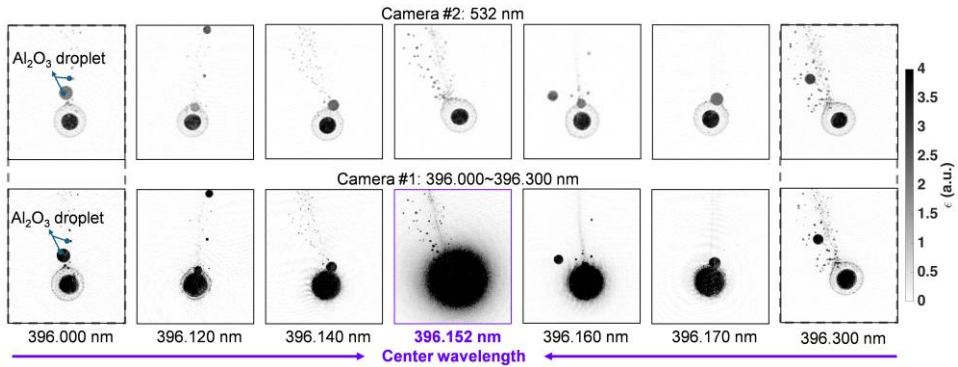
## 5.3 Aluminum atom profile around a burning droplet

Figure 5.11 presents typical snapshots of the extinction of burning aluminum droplets detected by the laser absorption spectroscopy. The top row displays shadowgraph images captured by camera #2 with back illumination at 532 nm. The bottom row shows the corresponding signal images from camera #1 which is



illuminated by the diode laser tuned from 396.000 to 396.300 nm. The light extinction in the top row results from the condensed-phase materials, including the central aluminum droplet and the alumina products, while the extinction in the bottom row originates from both the above condensed-phase materials and the Al atoms. The images in the top row serve as references to the aluminum droplet position for the corresponding bottom image.

In the bottom row, when the wavelength of the diode laser shifts from 396.000 to 396.152 nm (resonant wavelength), the region with extinction higher than four (more than 98% of light extinct) expands from the central aluminum droplet region to the region even outside of the alumina condensation layer (equivalent to the flame sheet, see Section 5.1). For example, at 396.000 nm, the bottom image shows only a slight difference compared to the image acquired at 532 nm, suggesting negligible aluminum atomic absorption at this wavelength. However, at the resonant wavelength of 396.152 nm, the high-extinction region ( $>4$ ) extends to positions where  $r/r_0$  exceeds three, while the alumina condensation layer is located around  $r/r_0 \approx 1.8$  (where  $r_0$  denotes the droplet radius). This indicates that aluminum atoms exist outside the flame sheet, contributing to strong absorption. When the central wavelength of the diode laser is tuned to 396.300 nm, the opposite trend is observed: the boundaries of the high-extinction regions contract from areas outside the flame sheet toward the surface of the central aluminum droplet. This contraction occurs because the concentration of aluminum atoms decreases radially from the center of the droplet. At off-resonant wavelengths, the absorption cross-section  $\sigma(\nu)$  diminishes, resulting in strong absorption only in regions with high aluminum concentrations.



**Figure 5.11:** Comparison of instantaneous absorbance measured simultaneously by camera #2 (532 nm CW laser, top) and camera #1 at different wavelengths (396.000–396.300 nm diode laser, bottom).

Moreover, the atomic absorption happens almost in the entire range from 396.000 to 396.300 nm at the position near the aluminum droplet surface. In this region, the absorption line width is around  $\pm 50$  GHz, which is much wider than the line width



( $\sim \pm 4$  GHz) reported by previous studies [77,86,98]. Compared to the previous studies under conditions of low temperature ( $\sim 400$  K) and low pressure ( $\sim 50$   $\mu$ bar), the temperature of the Al atoms in the current study reaches over 2600 K and the pressure is 1 atm. Higher temperatures and pressures significantly broaden the absorption line shape due to Doppler and collisional effects. Another feature is that no atomic absorption is observed around the alumina products at the tip of the flame sheet. This indicates these droplets are stable and there is no obvious dissociation generating Al atoms even at temperatures of around 3500 K.

The number density of Al atoms along the radius direction is shown in Figure 5.12. The quantification is conducted according to Eq. (4.7) in Section 4.3.2. However, as the laser light is completely absorbed at 396.152 nm in the region  $r/r_0 = 1.2 \sim 3.0$ , a peak absorbance is unavailable for the fitting of the Voigt profile. Therefore, we define the regions with  $r/r_0 \leq 3.0$  as optically thick regions, while the region with  $r/r_0 > 3.0$  is the optically thin region. In the optically thick region, the number density is determined by fitting the ‘wings’ of the absorbance following the Voigt profile, using a similar method introduced in previous studies [87,99]. Detailed fitting of the Voigt profiles for all the wavelengths can be referred to in **Paper IV**. Finally, the number density of Al atom drops from  $\sim 1.1 \times 10^{22} \text{ m}^{-3}$  at  $r/r_0 = 1.3$  to  $\sim 3.5 \times 10^{20} \text{ m}^{-3}$  at  $r/r_0 = 2.9$ . However, due to the limited datasets for optically thick conditions, the reconstructed absorption profiles might contain large uncertainties thus resulting in large errors in the results of Al number density. This can be improved by employing finer wavelength steps so that more data points can be obtained for the ‘wing’ in the absorption profiles to improve fitting accuracy. In the optically thin region, the Al concentration keeps dropping to  $\sim 7.0 \times 10^{19} \text{ m}^{-3}$  at  $r/r_0 = 4.9$ .

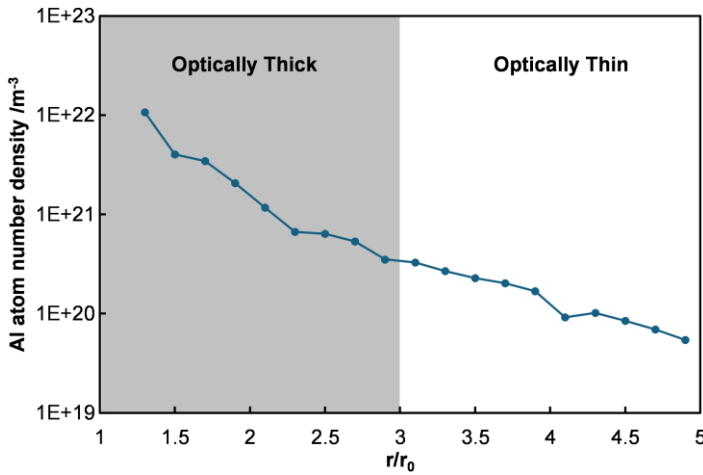


**Figure 5.12:** Aluminum atom distribution profile around a burning aluminum droplet with a diameter of around 240  $\mu\text{m}$ .

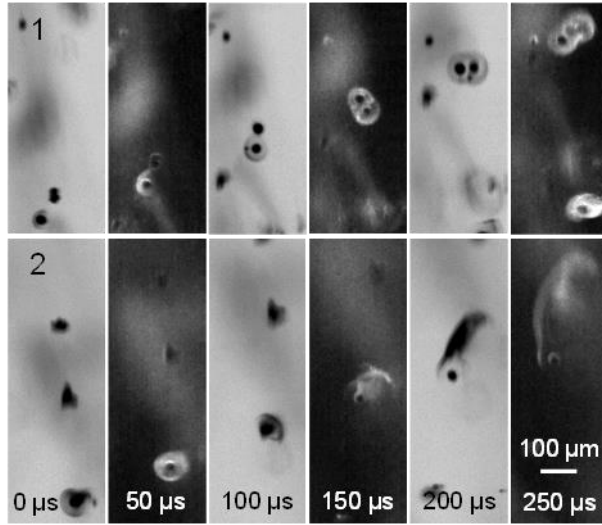
## 5.4 Nano-oxide formation in the dust flame

Figure 5.13 displays two sequences of consecutive transmission and scattered light images within the dust flame. In sequence 1 at 0  $\mu\text{s}$ , two aluminum particles are observed: the lower particle has just begun to melt and develop a flame, while the upper particle remains solid, as indicated by its irregular shape. At 50  $\mu\text{s}$ , light scattering reveals the expansion of hot alumina particles from the flame toward the solid upper aluminum particle, leading to its melting by 100  $\mu\text{s}$ , as shown by the spherical shadowgraph. By 150  $\mu\text{s}$ , scattered light surrounding the particle indicates the formation of the flame. Throughout the sequence, the two droplets remain close, with their flames partially overlapping. These observations illustrate a crucial ignition mechanism in dust flames with high particle concentrations: the deposition of hot alumina products onto the surfaces of aluminum particles melts the oxide coating, thereby igniting neighboring aluminum particles. This mechanism explains why the temperature of the heating source required to ignite a dust flame does not need to reach the alumina melting point. The high concentration of particle supply enhances particle–particle interactions, leading to the ignition and stabilization of aluminum dust flames. The particle-particle interaction is discussed in **Paper VI** and **Paper VII**.

Sequence 2 depicts an aluminum droplet transitioning from symmetric to asymmetric combustion. At 0  $\mu\text{s}$ , the flame in the lowest shadowgraph appears perturbed and partially extinguished on the right side of the droplet. This local extinction of the flame is thought to be attributed to the deposition of hot alumina particles ( $T \approx 3500$  K), which locally cover the cooler aluminum droplet ( $T \approx 2700$  K). At 100  $\mu\text{s}$ , the perturbed region abruptly shifts to the left side of the droplet, indicating a clockwise rotation. Between 150  $\mu\text{s}$  and 250  $\mu\text{s}$ , droplet eruption occurs, forming a condensation trail on the upper side of the aluminum droplet. Strong light extinction and light scattering of the trail are observed at 200  $\mu\text{s}$  and 250  $\mu\text{s}$ , respectively. The eruption results from the sudden and intense emergence of aluminum vapor due to the coalescence of alumina products. This behavior is similar to the jetting observed in the single isolated droplets shown in Figure 5.2 and discussed in **Paper III**. It is also important to note that nearly all aluminum droplets in the dust flame experience eruption approximately 100–300  $\mu\text{s}$  after ignition. Thus, droplet eruption is a significant event in the dust flame, generating large amounts of nanometer-sized particles.

Based on light extinction and scattering, quantification of the nanoparticles is conducted using a self-developed imaging processing scheme (details found in **Paper VII**). Figure 5.14 shows an example of the transmissions after (a) absorption and (b) scattering, (c) the single scattering albedo, and (d) the nanoparticle volume and (e) size. The nanoparticle particle size is around 50 nm close to the droplet and increases along the trail and to the sides of the nanoparticle region to around 100 nm.

Nanoparticles with diameters above 100 nm are rarely found. More examples showing the nanoparticle volume and size are presented in **Paper VII**.



**Figure 5.13:** Sequences of consecutive transmission and scattered-light images showing (1) particle melting, ignition, and collision, and (2) droplet eruption.

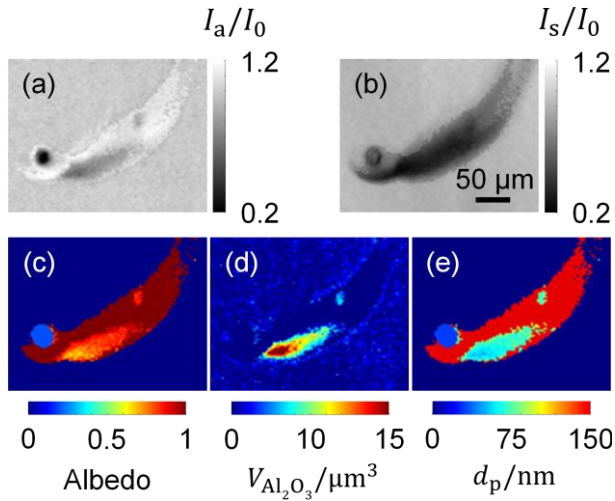


**Figure 5.14:** Transmission after (a) absorption and (b) scattering, (c) single-scattering albedo, (d) nanoparticle volume, and (e) size distribution.

# 6. Summary and outlook

## 6.1 Summary

This thesis presents different lab-scale aluminum flames and multiple optical diagnostic methods developed and applied for the characterization of aluminum droplet combustion. The novel design of aluminum combustion setups from individual micrometer droplets to collective particle dust provides stable targets for in-situ optical investigations. The established spatiotemporal optical techniques scrutinize aluminum combustion from different perspectives, including flame structure, combustion temperature, Al atom concentration, and nano-oxide formation.

To advance the understanding of the aluminum-steam reaction for the simultaneous production of heat and hydrogen, a combustion platform for single aluminum droplets burning in high-temperature steam was developed. A flat flame burner was modified to create an adjustable oxidizing environment, ranging from  $\text{H}_2\text{O}/\text{N}_2$  to  $\text{H}_2\text{O}/\text{O}_2/\text{N}_2$  mixtures. Integrated with an aluminum wire positioning device, this setup allows for the stable generation of individual burning aluminum droplets with good control over their initial size and combustion behavior. Aluminum droplets with diameters between approximately  $100\text{ }\mu\text{m}$  and  $500\text{ }\mu\text{m}$  are produced by varying the sizes of the aluminum wires used. Moreover, aluminum alloy wires were also used to study the effects of composition on combustion behaviors.

Besides, a lifted aluminum dust flame was established using fine aluminum powders (75%,  $D < 5\text{ }\mu\text{m}$ ). The powders are aerosolized by a high-voltage capacitor and carried by air into a flat methane flame at approximately 2000 K. By increasing the capacitor voltage to enhance the powder supply, the aluminum dust ignites and stabilizes. In contrast to the single droplet flame, this dust flame provides opportunities to study flame stabilization, particle-particle interactions, and nano-oxide formation.

In-situ characterization of burning aluminum droplets is challenging due to their intrinsic complexity in several aspects, such as nano-to-micrometer spatial scale, the transient process in milliseconds, multi-phase dynamics, and extremely high temperature. Several spatiotemporal optical diagnostic techniques were developed to study different key parameters:

- 1) High-speed incandescence-shadowgraph imaging. The technique captures the flame morphology evolution and condensed-phase droplet distribution simultaneously. The two complementary views help to determine key parameters, including the flame standoff distance, flame sheet thickness, evaporation rates, and Stefan flow velocity.
- 2) High-speed RGB pyrometry imaging. It spatially resolves the surface temperatures of different parts over a burning aluminum droplet, like the temperatures of the aluminum core, the alumina cap, and the alumina droplets on the flame sheet. Besides, temperature dynamics along the wire ignition process and the droplet development process are also studied.
- 3) Spatially resolved laser absorption spectroscopy on Al atom. The technique quantifies the Al atom concentration profile around a burning droplet.
- 4) Darkfield and brightfield microscopy. The technique captures the combustion behavior of individual particles within the dust flame. It quantifies the size and volume of nano-oxide particles ( $D < 130$  nm) in the condensation trail of a jetting aluminum droplet.

Overall, this thesis delivers key datasets and generates new knowledge that helps to advance the understanding of aluminum combustion.

## 6.2 Outlook

The use of aluminum as a fuel in clean energy cycles is an emerging field, with aluminum-steam combustion remaining relatively underexplored. This thesis studies aluminum droplet combustion in different aspects, however, more questions remain unexplored and require future efforts.

First, the emissivity of alumina droplets in nano-to-micrometer scales remains largely unknown. It is crucial for the determination of the burning temperature and thermal radiation power of aluminum flames. For example, the graybody assumption (constant emissivity) is often applied in the surface temperature measurements of alumina, which might cause large errors, especially for the nanometer particles. Thus, systematic investigations on the alumina emissivity particularly from nanometer to micrometer size in the range of 2000–4000 K are necessary. Second, the heat transfer of a burning aluminum droplet is still unclear. This thesis conducts a simplified analysis of heat transfer in single burning droplets based on experimentally determined evaporation rates. The findings indicate that conductive and radiative heat transfer are insufficient to provide the latent heat of evaporation. This discrepancy suggests that surface reactions producing gaseous oxide species may play significant roles. Future theoretical studies should incorporate chemical kinetics to develop a comprehensive heat balance model for

single aluminum droplet combustion. Furthermore, alumina condensation is a critical process that requires detailed experimental investigation. Building on the single aluminum droplet studies in the thesis, in-situ quantification of alumina particle formation on the flame sheet, such as growth rates and size distributions, could enhance the understanding of condensation mechanisms. Additionally, intermediate species like Al and AlO are essential for elucidating the chemical kinetics of aluminum combustion. While this thesis quantifies Al atoms using laser absorption spectroscopy, it encounters challenges due to strong resonant absorption, which leads to complete extinction near the aluminum droplet surface and results in high uncertainty in Al atom number density measurements. Future efforts should focus on optimizing measurement techniques to improve accuracy. Furthermore, laser absorption spectroscopy of AlO offers a promising approach for determining the AlO concentration profile.

Moreover, additional advanced laser/optical diagnostics are promising and available for the characterization of aluminum combustion in the future, as summarized in the latest review by M. Aldén [100]. Techniques such as Raman scattering could be utilized to measure major components like  $H_2$ ,  $H_2O$ , and  $N_2$ , while single- and two-photon absorption laser-induced fluorescence (LIF) can enable the detection of essential radicals including AlO, OH, Al, O, and H. Tomography could facilitate three-dimensional reconstruction of combustion processes, and Rayleigh scattering is able to be employed to measure the gaseous temperature field. Particularly, incorporating Structured Illumination strategies into these advanced techniques would be favorable for suppressing interference from sources such as laser scattering and thermal radiation, thereby significantly improving the signal-to-noise ratio in aluminum combustion studies. Additionally, the integration of ultrafast (ps/fs) lasers into these methods would be desirable for detecting transient events during aluminum combustion.

Additionally, experimental investigations into aluminum combustion typically begin with the development of particle combustion facilities. Future efforts should emphasize the establishment of standardized combustion setups across various scales. A well-designed combustion platform can significantly mitigate the challenges associated with flame characterization. For example, precise control of particle seeding in single-particle combustion or dust flame is crucial for generating stable and controllable aluminum flames as research targets. Besides, standardized setups should accommodate key variables such as particle size, oxidizer type ( $H_2O$ ,  $O_2$ ,  $CO_2$ , etc.), temperature, and pressure, thereby enabling systematic database development and facilitating comparisons among different research groups.

# References

- [1] J. Rising, M. Tedesco, F. Piontek, D.A. Stainforth, The missing risks of climate change, *Nature*. 610 (2022) 643–651.
- [2] N. Kittner, F. Lill, D.M. Kammen, Energy storage deployment and innovation for the clean energy transition, *Nat. Energy*. 2 (2017) 17125.
- [3] A. Cherp, V. Vinichenko, J. Tosun, J.A. Gordon, J. Jewell, National growth dynamics of wind and solar power compared to the growth required for global climate targets, *Nat. Energy*. 6 (2021) 742–754.
- [4] J. Zhao, F. Li, Q. Zhang, Impacts of renewable energy resources on the weather vulnerability of power systems, *Nat. Energy*. 9 (2024) 1407–1414.
- [5] J.M. Bergthorson, S. Goroshin, M.J. Soo, P. Julien, J. Palecka, D.L. Frost, D.J. Jarvis, Direct combustion of recyclable metal fuels for zero-carbon heat and power, *Appl. Energy*. 160 (2015) 368–382.
- [6] J.M. Bergthorson, Y. Yavor, J. Palecka, W. Georges, M. Soo, J. Vickery, S. Goroshin, D.L. Frost, A.J. Higgins, Metal-water combustion for clean propulsion and power generation, *Appl. Energy*. 186 (2017) 13–27.
- [7] J.M. Bergthorson, Recyclable metal fuels for clean and compact zero-carbon power, *Prog. Energy Combust. Sci.* 68 (2018) 169–196.
- [8] F. Halter, S. Jeanjean, C. Chauveau, Y. Berro, M. Balat-Pichelin, J.F. Brillhac, A. Andrieu, C. Schonnenbeck, G. Leyssens, C. Dumand, Recyclable metal fuels as future zero-carbon energy carrier, *Appl. Energy Combust. Sci.* 13 (2023) 100100.
- [9] J. Janicka, P. Debiagi, A. Scholtissek, A. Dreizler, B. Eppele, R. Pawellek, A. Maltsev, C. Hasse, The potential of retrofitting existing coal power plants: A case study for operation with green iron, *Appl. Energy*. 339 (2023) 120950.
- [10] K.A. Trowell, S. Goroshin, D.L. Frost, J.M. Bergthorson, Aluminum and its role as a recyclable, sustainable carrier of renewable energy, *Appl. Energy*. 275 (2020) 115112.
- [11] I.R. Souza Filho, H. Springer, Y. Ma, A. Mahajan, C.C. da Silva, M. Kulse, D. Raabe, Green steel at its crossroads: Hybrid hydrogen-based reduction of iron ores, *J. Clean. Prod.* 340 (2022) 130805.
- [12] S. Fischer, M. Grubelich, Theoretical energy release of thermites, intermetallics, and combustible metals, SAND98-1176C, Sandia National Laboratories, Albuquerque, United States, 1998.
- [13] X. Yu, N.S. Sandhu, Z. Yang, M. Zheng, Suitability of energy sources for automotive application – A review, *Appl. Energy*. 271 (2020) 115169.

- [14] E.I. Shkolnikov, A.Z. Zhuk, M.S. Vlaskin, Aluminum as energy carrier: Feasibility analysis and current technologies overview, *Renew. Sustain. Energy Rev.* 15 (2011) 4611–4623.
- [15] P. Boudreau, M. Johnson, J.M. Bergthorson, Techno-economic assessment of aluminum as a clean energy carrier to decarbonize remote industries, *Energy Adv.* 3 (2024) 1919–1931.
- [16] R.A. Yokel, B. Sjögren, *Handbook on the Toxicology of Metals* (5th Edition), Chapter 1, Aluminum, Elsevier B.V., 2021.
- [17] N.E. Carlucci, A.P. Shaw, M.D. Motyka, J.C. Poret, K.M. Westerkamp, Apparatus and Method for High-Throughput Screening of Pyrotechnic Compositions, Propellants, Explos. Pyrotech. 50 (2024) e202400136.
- [18] H.R. Pourtedal, M.H. Roudashti, Thermal behavior of metallic fuel pyrotechnics of Al, Mg and alloy of Al–Mg: a review, *J. Therm. Anal. Calorim.* 149 (2024) 12635–12650.
- [19] X. Liao, J. Pei, P. Xie, Y. Hu, J. Liu, Aluminum particle agglomeration characteristics and suppression method during the combustion of aluminum-based solid propellants: A review, *Propellants, Explos. Pyrotech.* 49 (2024) 1–13.
- [20] T.L. Pourpoint, T.D. Wood, M.A. Pfeil, J. Tsohas, S.F. Son, Feasibility study and demonstration of an aluminum and ice solid propellant, *Int. J. Aerosp. Eng.* 2012 (2012) 874076.
- [21] Q. Pontalier, J. Loiseau, S. Goroshin, F. Zhang, D.L. Frost, Blast enhancement from metalized explosives, *Shock Waves*. 31 (2021) 203–230.
- [22] S. Goroshin, D.L. Frost, J. Levine, A. Yoshinaka, F. Zhang, Optical pyrometry of fireballs of metalized explosives, *Propellants, Explos. Pyrotech.* 31 (2006) 169–181.
- [23] J.P. Foote, B.R. Thompson, J.T. Lineberry, Combustion of aluminum with steam for underwater propulsion, *Advances in Chemical Propulsion*, Chapter 8 (2001) 133–146.
- [24] D.F. Waters, C.P. Cadou, Modeling a hybrid Rankine-cycle/fuel-cell underwater propulsion system based on aluminum-water combustion, *J. Power Sources*. 221 (2013) 272–283.
- [25] M.S. Vlaskin, E.I. Shkolnikov, A. V. Bersh, A.Z. Zhuk, A. V. Lisicyn, A.I. Sorokovikov, Y. V. Pankina, An experimental aluminum-fueled power plant, *J. Power Sources*. 196 (2011) 8828–8835.
- [26] K.A. Trowell, S. Goroshin, D.L. Frost, J.M. Bergthorson, The use of supercritical water for the catalyst-free oxidation of coarse aluminum for hydrogen production, *Sustain. Energy Fuels*. 4 (2020) 5628–5635.
- [27] F. Halter, D. Keo, B. Grosselin, E. Schweers, L. Portugues, N. Windhab, *International Journal of Hydrogen Energy*. Demonstration of the co-generation of heat and hydrogen by high-temperature oxidation of aluminum in steam, *Int. J. Hydrogen Energy*. 102 (2025) 1140–1142.
- [28] I. Glassman, R.A. Yetter, N.G. Glumac, *Combustion*, Academic Press, 2014.
- [29] E.L. Dreizin, Phase changes in metal combustion, *Prog. Energy Combust. Sci.* 26 (2000) 57–78.



- [30] R. Lomba, P. Laboureur, C. Dumand, C. Chauveau, F. Halter, Determination of aluminum-air burning velocities using PIV and Laser sheet tomography, *Proc. Combust. Inst.* 37 (2019) 3143–3150.
- [31] S. Goroshin, J. Mamen, A. Higgins, T. Bazyn, N. Glumac, H. Krier, Emission spectroscopy of flame fronts in aluminum suspensions, *Proc. Combust. Inst.* 31 (2007) 2011–2019.
- [32] C.L. Yeh, K.K. Kuo, Ignition and combustion of boron particles, *Prog. Energy Combust. Sci.* 22 (1996) 511–541.
- [33] K.L. Chintersingh, M. Schoenitz, E.L. Dreizin, Combustion of boron and boron–iron composite particles in different oxidizers, *Combust. Flame.* 192 (2018) 44–58.
- [34] D. Ning, Y. Shoshin, M. van Stiphout, J. van Oijen, G. Finotello, P. de Goey, Temperature and phase transitions of laser-ignited single iron particle, *Combust. Flame.* 236 (2022) 111801.
- [35] L.C. Thijs, D. Ning, Y.S. Shoshin, T. Hazenberg, X.C. Mi, J.A. van Oijen, P. de Goey, Temperature evolution of laser-ignited micrometric iron particles: A comprehensive experimental data set and numerical assessment of laser heating impact, *Appl. Energy Combust. Sci.* 19 (2024) 100284.
- [36] D.S. Sundaram, P. Puri, V. Yang, A general theory of ignition and combustion of nano- and micron-sized aluminum particles, *Combust. Flame.* 169 (2016) 94–109.
- [37] A. Braconnier, S. Gallier, F. Halter, C. Chauveau, Aluminum combustion in CO<sub>2</sub>-CO-N<sub>2</sub> mixtures, *Proc. Combust. Inst.* 38 (2021) 4355–4363.
- [38] A. Braconnier, C. Chauveau, F. Halter, S. Gallier, Experimental investigation of the aluminum combustion in different O<sub>2</sub> oxidizing mixtures: Effect of the diluent gases, *Exp. Therm. Fluid Sci.* 117 (2020) 110110.
- [39] C. Badiola, R.J. Gill, E.L. Dreizin, Combustion characteristics of micron-sized aluminum particles in oxygenated environments, *Combust. Flame.* 158 (2011) 2064–2070.
- [40] R.J. Gill, C. Badiola, E.L. Dreizin, Combustion times and emission profiles of micron-sized aluminum particles burning in different environments, *Combust. Flame.* 157 (2010) 2015–2023.
- [41] P. Bucher, R.A. Yetter, F.L. Dryer, T.P. Parr, D.M. Hanson-Parr, Plif species and ratiometric temperature measurements of aluminum particle combustion in O<sub>2</sub>, CO<sub>2</sub> and N<sub>2</sub>O oxidizers, and comparison with model calculations, *Symp. Combust.* 27 (1998) 2421–2429.
- [42] P. Bucher, R.A. Yetter, F.L. Dryer, T.P. Parr, D.M. Hanson-Parr, E.P. Viceni, Flames structure measurement of single, isolated aluminum particles burning in air, *Proc. Combust. Inst.* 26 (1996) 1899–1908.
- [43] Y. Tang, W. Dong, X. Zou, B. Shi, N. Wang, Ignition and combustion of a dense powder jet of micron-sized aluminum particles in hot gas, *Proc. Combust. Inst.* 39 (2023) 3625–3636.
- [44] A. Corcoran, S. Mercati, H. Nie, M. Milani, L. Montorsi, E.L. Dreizin, Combustion of fine aluminum and magnesium powders in water, *Combust. Flame.* 160 (2013) 2242–2250.

- [45] Y. Feng, Z. Xia, L. Huang, L. Ma, Ignition and combustion of a single aluminum particle in hot gas flow, *Combust. Flame*. 196 (2018) 35–44.
- [46] E.L. Dreizin, Experimental study of stages in aluminum particle combustion in air, *Combust. Flame*. 105 (1996) 541–556.
- [47] Y. Tang, C. Li, B. Huang, B. Shi, N. Wang, Burning of aluminum particles assisted by selective energy coupling with a microwave plasma torch, *Proc. Combust. Inst.* 40 (2024) 105324.
- [48] K.P. Brooks, M.W. Beckstead, Dynamics of aluminum combustion, *J. Propuls. Power*. 11 (1995) 769–780.
- [49] C. Da Wen, I. Mudawar, Emissivity characteristics of polished aluminum alloy surfaces and assessment of multispectral radiation thermometry (MRT) emissivity models, *Int. J. Heat Mass Transf.* 48 (2005) 1316–1329.
- [50] P. Lynch, H. Krier, N. Glumac, Emissivity of aluminum-oxide particle clouds: Application to pyrometry of explosive fireballs, *J. Thermophys. Heat Transf.* 24 (2010) 301–308.
- [51] S. Gallier, A. Braconnier, F. Godfroy, F. Halter, C. Chauveau, The role of thermophoresis on aluminum oxide lobe formation, *Combust. Flame*. 228 (2021) 142–153.
- [52] M.W. Beckstead, Y. Liang, K. V. Puddupakkam, Numerical simulation of single aluminum particle combustion (review), *Combust. Explos. Shock Waves*. 41 (2005) 622–638.
- [53] P. Bucher, L. Ernst, F.L. Dryer, R.A. Yetter, T.P. Parr, D.M. Hanson-Parr, Detailed Studies on the Flame Structure of Aluminum Particle Combustion, *Am. Inst. Aeronaut. Astronaut.* (2000) 689–722.
- [54] Y. Zhang, X. Xie, C. Chen, H. Li, J. Yi, Y. Xu, Z. Sun, F. Zhao, A Review on the Gas-Phase Modeling Study of Aluminum Combustion in Various Environments, *Propellants, Explos. Pyrotech.* (2024) 1–15.
- [55] L. Catoire, J.F. Legendre, M. Giraud, Kinetic model for aluminum-sensitized ram accelerator combustion, *J. Propuls. Power*. 19 (2003) 196–202.
- [56] Y. Huang, G.A. Risha, V. Yang, R.A. Yetter, Analysis of nano-aluminum particle dust cloud combustion in different oxidizer environments, 43rd AIAA Aerospace Sciences Meeting and Exhibit. (2005) 0738.
- [57] E.B. Washburn, J.N. Trivedi, L. Catoire, M.W. Beckstead, The simulation of the combustion of micrometer-sized aluminum particles with steam, *Combust. Sci. Technol.* 180 (2008) 1502–1517.
- [58] A.M. Starik, P.S. Kuleshov, A.S. Sharipov, N.S. Titova, C.J. Tsai, Numerical analysis of nanoaluminum combustion in steam, *Combust. Flame*. 161 (2014) 1659–1667.
- [59] P. Bucher, R.A. Yetter, F.L. Dryer, E.P. Vicenzi, T.P. Parr, D.M. Hanson-Parr, Condensed-phase species distributions about Al particles reacting in various oxidizers, *Combust. Flame*. 117 (1999) 351–361.
- [60] F. Halter, V. Glasziou, M. Di Lorenzo, S. Gallier, C. Chauveau, Peculiarities of aluminum particle combustion in steam, *Proc. Combust. Inst.* 39 (2023) 3605–3614.

- [61] G. Vilmart, N. Dorval, R. Devillers, Y. Fabignon, B. Attal-Trétout, A. Bresson, Imaging aluminum particles in solid-propellant flames using 5 kHz LIF of Al atoms, *Materials*. 12 (2019) 2421.
- [62] V.B. Storozhev, A.N. Yermakov, Combustion of nano-sized aluminum particles in steam: Numerical modeling, *Combust. Flame*. 162 (2015) 4129–4137.
- [63] V.B. Storozhev, A.N. Yermakov, Effect of suboxides on dynamics of combustion of aluminum nanopowder in water vapor: Numerical estimate, *Combust. Flame*. 190 (2018) 103–111.
- [64] M.W. Beckstead, *A Summary of Aluminum Combustion*, Provo, Utah, USA, 2004.
- [65] J. Finke, F. Sewerin, A population balance approach for predicting the size distribution of oxide smoke near a burning aluminum particle, *Combust. Flame*. 265 (2024) 113464.
- [66] J. Glorian, S. Gallier, L. Catoire, On the role of heterogeneous reactions in aluminum combustion, *Combust. Flame*. 168 (2016) 378–392.
- [67] J. Zhang, Z. Xia, O.T. Stein, L. Ma, F. Li, Y. Feng, Z. Zhang, A. Kronenburg, Combustion characteristics of aluminum particle jet flames in a hot co-flow, *Chem. Eng. J.* 442 (2022) 135876.
- [68] I. González de Arrieta, C. Blanchard, P. Laboureur, C. Chauveau, C. Genevois, O. Rozenbaum, F. Halter, Radiative properties of micron-sized Al/air premixed flames described by an effective medium core-shell formulation, *Int. J. Heat Mass Transf.* 203 (2023) 123815.
- [69] V. Glasziou, C. Chauveau, S. Courtiaud, F. Halter, Measurement of the temperature of burning aluminum particles using multi-spectral pyrometry, *Combust. Sci. Technol.* 196 (2024) 2138–2151.
- [70] Y. Tang, X. Zou, W. Dong, B. Shi, N. Wang, S. Li, Temperature measurements and high-speed photography of micron-sized aluminum particles burning in methane flat-flame exhaust, *Fuel*. 306 (2021) 121743.
- [71] Y. Chen, D.R. Gueldenbecher, K.N.G. Hoffmeister, M.A. Cooper, H.L. Stauffacher, M.S. Oliver, E.B. Washburn, Study of aluminum particle combustion in solid propellant plumes using digital in-line holography and imaging pyrometry, *Combust. Flame*. 182 (2017) 225–237.
- [72] T.L. Bergman, A.S. Lavine, F.P. Incropera, D.P. Dewitt, *Fundamentals of Heat and Mass transfer*, 7th ed, John Wiley & Sons, Inc., 2011.
- [73] C.F. Bohren, D.R. Huffman, *Absorption and Scattering of Light by Small Particles*, John Wiley & Sons, Inc., 1989.
- [74] N.I. Poletaev, A. V. Florko, Radiative characteristics of an aluminum dust flame. Condensed phase, *Combust. Explos. Shock Waves*. 43 (2007) 414–422.
- [75] J. Kalman, D. Allen, N. Glumac, H. Krier, Optical depth effects on aluminum oxide spectral emissivity, *J. Thermophys. Heat Transf.* 29 (2015) 74–82.
- [76] NIST(National Institute of Standards and Technology), *Handbook of Basic Atomic Spectroscopic Data*, (2024).

- [77] J. Olejnicek, H.T. Do, Z. Hubicka, R. Hippler, L. Jastrabik, Blue Diode Laser Absorption Spectroscopy of Pulsed Magnetron Discharge, *Jpn. J. Appl. Phys.* 45 (2006) 8090.
- [78] O. Launila, L.E. Berg, Spectroscopy of AlO: Combined analysis of the  $A^2\Pi_i \rightarrow X^2\Sigma^+$  and  $B^2\Sigma^+ \rightarrow X^2\Sigma^+$  transitions, *J. Mol. Spectrosc.* 265 (2011) 10–14.
- [79] N. Glumac, H. Krier, T. Bazyn, R. Ever, Temperature measurements of aluminum particles burning in carbon dioxide, *Combust. Sci. Technol.* 177 (2005) 485–511.
- [80] M. Soo, S. Goroshin, N. Glumac, K. Kumashiro, J. Vickery, D.L. Frost, J.M. Bergthorson, Emission and laser absorption spectroscopy of flat flames in aluminum suspensions, *Combust. Flame.* 180 (2017) 230–238.
- [81] Flat Flame Burner, Holthuis and Associates, PO Box 2554, Sebastopol, CA 95473, USA. <http://www.flatflame.com>.
- [82] A. Braconnier, C. Chauveau, F. Halter, S. Gallier, Detailed analysis of combustion process of a single aluminum particle in air using an improved experimental approach, *Int. J. Energ. Mater. Chem. Propuls.* 17 (2018) 111–124.
- [83] A. Araújo, Multi-spectral pyrometry - a review, *Meas. Sci. Technol.* 28 (2017) 082002.
- [84] J.C. De Vos, A new determination of the emissivity of tungsten ribbon, *Physica.* 3 (1954) 690–714.
- [85] R.D. Larrabee, Spectral Emissivity of Tungsten, *J. Opt. Soc. Am.* 49 (1959) 619–625.
- [86] M. Wolter, H.T. Do, H. Steffen, R. Hippler, Aluminium atom density and temperature in a dc magnetron discharge determined by means of blue diode laser absorption spectroscopy, *J. Phys. D. Appl. Phys.* 38 (2005) 2390–2395.
- [87] W. Weng, C. Brackmann, T. Leffler, M. Aldén, Z. Li, Ultraviolet Absorption Cross Sections of KOH and KCl for Nonintrusive Species-Specific Quantitative Detection in Hot Flue Gases, *Anal. Chem.* 91 (2019) 4719–4726.
- [88] E.E. Whiting, An empirical approximation to the Voigt profile, *J. Quant. Spectrosc. Radiat. Transf.* 8 (1968) 1379–1384.
- [89] F. Liu, J. Yon, A. Fuentes, P. Lobo, G.J. Smallwood, J.C. Corbin, Review of recent literature on the light absorption properties of black carbon: Refractive index, mass absorption cross section, and absorption function, *Aerosol Sci. Technol.* 54 (2020) 33–51.
- [90] J. Zhu, M.Y. Choi, G.W. Mulholland, S.L. Manzello, L.A. Gritzo, J. Suo-Anttila, Measurement of visible and near-IR optical properties of soot produced from laminar flames, *Proc. Combust. Inst.* 29 (2002) 2367–2374.
- [91] P. Laven, MiePlot (A computer program for scattering of light from a sphere using Mie theory & the Debye series), <http://www.philiplaven.com/mieplot.htm>, (2011).
- [92] M.W. Chase, NIST-JANAF Thermochemical Tables, 4th ed, *J. Phys. Chem. Ref. Data.* (1998).
- [93] D.R. Lide, *CRC Handbook of Chemistry and Physics*, CRC press, 2005.
- [94] K.K. Kuo, *Principles of Combustion*, John Wiley & Sons, Inc., 2005.

- [95] N.C. Blais, J.B. Mann, Thermal conductivity of helium and hydrogen at high temperatures, *J. Chem. Phys.* 32 (1960) 1459–1465.
- [96] S.C. Saxena, S.H.P. Chen, Thermal conductivity of nitrogen in the temperature range 350–2500 K, *Mol. Phys.* 29 (1975) 1507–1519.
- [97] B.J. McBride, NASA Glenn coefficients for calculating thermodynamic properties of individual species, <https://cearun.grc.nasa.gov/ThermoBuild/>, (2002).
- [98] H. Scheibner, S. Franke, S. Solyman, J.F. Behnke, C. Wilke, A. Dinklage, Laser absorption spectroscopy with a blue diode laser in an aluminum hollow cathode discharge, *Rev. Sci. Instrum.* 73 (2002) 378.
- [99] Z. Qu, E. Steinvall, R. Ghorbani, F.M. Schmidt, Tunable Diode Laser Atomic Absorption Spectroscopy for Detection of Potassium under Optically Thick Conditions, *Anal. Chem.* 88 (2016) 3754–3760.
- [100] M. Aldén, Spatially and temporally resolved laser/optical diagnostics of combustion processes: From fundamentals to practical applications, *Proc. Combust. Inst.* 39 (2023) 1185–1228.



